

UNIVERSITY OF LEEDS

DOCTORAL THESIS

Simulating the thermal conductivity of lower mantle minerals

Author:

Ben TODD

Supervisor:

Dr. Stephen STACKHOUSE

Dr. Andrew M. WALKER

Dr. Jon E. MOUND

A thesis submitted in fulfillment of the requirements

for the degree of Doctor of Philosophy

in the

Institute of Geophysics and Tectonics

School of Earth and Environment

March 4, 2019

Declaration of Authorship

I, Ben TODD, declare that this thesis titled, “Simulating the thermal conductivity of lower mantle minerals” and the work presented in it are my own. I confirm that:

- This work was done wholly or mainly while in candidature for a research degree at this University.
- Where any part of this thesis has previously been submitted for a degree or any other qualification at this University or any other institution, this has been clearly stated.
- Where I have consulted the published work of others, this is always clearly attributed.
- Where I have quoted from the work of others, the source is always given. With the exception of such quotations, this thesis is entirely my own work.
- I have acknowledged all main sources of help.
- Where the thesis is based on work done by myself jointly with others, I have made clear exactly what was done by others and what I have contributed myself.

Signed:

Date:

Do it!
Just do it!

Don't let your dreams be dreams.
Yesterday you said tomorrow, so just do it!
Make your dreams come true!
Just do it!

Some people dream of success,
while you're gonna wake up,
and work hard at it!
Nothing is impossible!

You should get to the point,
where anyone else would quit,
and you're not going to stop there.
No, what are you waiting for?

Do it!
Just do it!
Yes you can!
Just do it!

If you're tired of starting over,
stop
giving
up.

Shia LeBeouf

UNIVERSITY OF LEEDS

Abstract

Faculty of Environment

School of Earth and Environment

Doctor of Philosophy

Simulating the thermal conductivity of lower mantle minerals

by Ben TODD

The Thesis Abstract is written here (and usually kept to just this page). The page is kept centered vertically so can expand into the blank space above the title too...

Acknowledgements

The acknowledgments and the people to thank go here, don't forget to include your project advisor...

Everyone is smart, set yourself apart by being kind.

Contents

Declaration of Authorship	iii
Abstract	vii
Acknowledgements	ix
1 Thermal conductivity and the Earth's interior	1
1.1 Introduction to the problem	1
1.1.1 Man-made applications with thermal conductivity	1
1.1.2 Conductivity in the Earth	2
1.1.3 AIMS / WHAT DO I DO THAT IS DIFFERENT TO OTHERS	2
1.2 Structure of the Earth	3
1.2.1 Lower mantle	3
1.2.2 Above the lower mantle	4
1.2.3 Below the lower mantle	5
1.3 Defining thermal conductivity	5
1.3.1 Mechanisms of heat transport	6
Electron	6
Photon	6
Phonon	7
1.3.2 What affects it?	7
1.4 Previous work - geophysics	8
1.4.1 STUFF THAT IS INFLUENCED BY CONDUCTIVITY	8
Mantle dynamics	8
Heat flow	9
Geomagnetism	9
1.4.2 DETERMINATIONS OF TC FOR EARTH MATERIALS/CONDITIONS	10

	Experiments	10
	Calculations	11
	Radiative conductivity	13
1.5	Thesis outline	15
1.5.1	Aims	15
1.5.2	Objectives	15
2	Intro/Background/Theory 2	17
2.1	Atomic-scale modelling	17
2.1.1	Molecular dynamics	17
	Parameter drift/convergence	17
2.1.2	Interatomic potentials / Atomic interactions?	18
2.1.3	LAMMPS	18
2.1.4	DFT/other	18
2.2	Computing thermal conductivity	18
2.2.1	Finite-size effects	19
2.2.2	Direct method	20
	System setup	20
	Data processing	21
	Finite-size effects	22
	Other NEMD	23
2.2.3	Green-Kubo	24
2.2.4	Other	26
2.3	Previous work	26
2.3.1	Method comparison	26
2.3.2	Finite-size effects	26
	STUFF THAT MIGHT BE WRONG BECAUSE FSE?	26
3	Constraining the finite-size effects of molecular dynamics methods to compute thermal conductivity	27
3.1	Introduction	27
3.1.1	Finite-size effects	28
3.2	Computational approaches	28

3.2.1	Direct method	28
3.2.2	Green-Kubo	29
3.3	Results	31
3.3.1	Green-Kubo	31
3.3.2	Direct method	31
3.4	Summary	32
4	Modelling the thermal conductivity of Fe-bearing bridgmanite at the CMB	35
4.1	Simulating the effect of atomic impurities	35
4.1.1	How do impurities affect conductivity?	36
	ω_0/ω_D overview	37
	What effects the magnitude of impurity scattering?	37
4.1.2	ω and τ in depth	38
4.2	Methodology	41
4.2.1	How does iron behave?	41
4.2.2	Where do the impurities go?	42
4.3	Results	43
4.4	Parameterising composition and temperature effects on CMB conductivity	47
4.4.1	Parameterising the data fit	47
	Compositional dependence	48
	Why does this model work?	50
	Temperature dependence	52
4.4.2	MEAN FREE PATH	54
	MFP FROM DM EXTRAPOLATION	54
	SCALING MFP TO QUANTIFY PHONON-DEFECT SCATTERING	56
	C(1-C) MODEL LIMITATIONS	57
	DM ANALYSIS - PH-B SCATTERING AND SHORTEST CELL	57
	MASS VS. POTENTIAL IN MODELLING FE	57
5	Modelling the lower mantle with variable thermal conductivity	59
5.1	Main Section 1	59

5.1.1 Subsection 1	59
6 Summary/Discussion/Conclusion	61
6.1 Main Section 1	61
6.1.1 Subsection 1	61
A Frequently Asked Questions	63
A.1 How do I change the colors of links?	63
Bibliography	65

List of Figures

1.1	Thermal conductivity against Fe-content	13
2.1	The unit cell represents the smallest box of atoms that can be replicated to produce a crystal structure. A supercell is an arrangement of unit cells.	21
2.2	Movement and distribution of heat in the direct method. Orange to white scale represents temperature (modified from Stackhouse et al., 2015).	22
2.3	Idealised example of linear extrapolation procedure. Inverse computed conductivities are plotted against inverse simulation lengths. Extrapolation to y-axis gives conductivity of an infinite system length, i.e. the bulk material.	22
2.4	Normalised ACF. Correlation is taken over a longer length than shown on this plot (100 ps), however the function decays to less than 1% of its initial value at 2 ps. It continues to oscillate about zero, with a positive average value.	24
2.5	Integrated ACF, multiplied by constants to get thermal conductivity. Large variation in the first 1 ps corresponds to the correlation time where the ACF is unconverged (still decaying / large oscillations). Thermal conductivity is averaged from correlation time of 5 ps - 10 ps (region in red box).	25
4.1	CONTENTS BIT	39
4.2	CONTENTS BIT	44
4.3	CONTENTS BIT	45
4.4	CONTENTS BIT	46

4.5	CONTENTS BIT	46
4.6	CONTENTS BIT	49
4.7	CONTENTS BIT	50
4.8	CONTENTS BIT	52
4.9	CONTENTS BIT	54

List of Tables

4.1	CONTENTS BIT	42
4.2	CONTENTS BIT	49
4.3	CONTENTS BIT	55

List of Abbreviations

CMB	Core-mantle boundary
LLSVP	Large, low-shear-velocity province
ULVZ	Ultra low velocity zone
TBL	Thermal boundary layer
DAC	Diamond anvil cell
MgSiO₃	Magnesium Silicate
FeSiO₃	Iron Silicate
bdg	bridgmanite
pv	perovskite
ppv	post-perovskite
LAMMPS	Large-scale Atomic/Molecular Massively Parallel Simulator
DFT	Density Functional Theory
MD	Molecular Dynamics
EMD	Equilibrium Molecular Dynamics
NEMD	Non-equilibrium Molecular Dynamics
DM	Direct Method
GK	Green-Kubo
ACF	Auto-correlation function
MFP	Mean free path
FSE	Finite-size effects
BPT	Ballistic phonon transport

Physical Constants

Boltzmann constant $k_B = 1.380\,648\,528 \times 10^{-23} \text{ J K}^{-1}$

Boltzmann constant $k_B = 8.617\,330\,350 \times 10^{-5} \text{ eV/K}$

List of Symbols

a	distance	m
P	power	W (J s ⁻¹)
ω	angular frequency	rad

For/Dedicated to/To my...

Chapter 1

Thermal conductivity and the Earth's interior

1.1 Introduction to the problem

The nature of heat transport within a substance is controlled by its thermal conductivity. This influences the thermal evolution and heat budget of the Earth, but is poorly constrained across relevant conditions. Experiments can measure the conductivity of material, but not at the high pressure/temperature conditions found in the deep Earth. Computer simulations allow materials and their conductivities to be modelled on an atomic-scale, but care must be taken to achieve accurate results. This involves setting up the material to faithfully replicate its expected real-world counterpart, and choosing a simulation method which includes realistic atomic interactions. In this chapter, I will introduce thermal conductivity and the deep earth, considering the effects of the former on the latter.

1.1.1 Man-made applications with thermal conductivity

Knowledge of the thermal conductivity of solids is key in a wide range of technological applications, in addition to developing our understanding of natural systems. Low conductivities are required in thermoelectric materials, to maximise the efficiency of heat-electricity conversion (Snyder and Toberer, 2008). Thermal conductivity determines whether a material is a conductor or insulator of heat, both of which have many technological applications.

!!! SOLAR PANELS ETC.?

!!! FLESH OUT !!!

1.1.2 Conductivity in the Earth

Within the lower mantle, thermal conductivity influences the rate at which heat is transferred from core cooling towards the surface, and more importantly the mechanisms by which it does so (Lay et al., 2008). High thermal conductivity systems will preferentially transport heat by conduction. Systems will convect (ADVECT?) where there is too much heat to be transported by conduction alone (i.e. low conductivity conditions).

Observations of plume structures and cyclic subduction patterns (see Garnero and McNamara, 2008) suggest convective behaviour in the lower mantle. Thermal conductivity is poorly constrained in this region, obtaining a comprehensive depth profile is not a trivial task. Additional difficulties are pressure, temperature, and compositional dependences, including isotopic variation (Tang and Dong, 2010; Dalton et al., 2013; Tang et al., 2014) and inclusion of impurities (Manthilake et al., 2011; Ammann et al., 2014; Ohta et al., 2014).

1.1.3 AIMS / WHAT DO I DO THAT IS DIFFERENT TO OTHERS

The aim of the work presented in this thesis is to model thermal conductivity at the core mantle boundary (CMB). I will running simulations at high pressure and varying temperatures, considering the effects of composition across an entire solid solution.

By parameterising the temperature and compositional-dependence, thermal conductivity can be determined as a function of both at any condition. This is of particular use to LEMA because of REASONS.

In order to perform this parameterisation, I will need to explore the equations that describe these dependencies, adapting them where necessary to compliment my result set.

Working on the atomic-scale, compositional variations are more important than in a sample of bulk material. A relatively low amount of possible sites for impurities

to be placed means clumping is possible, and must be considered when randomly substituting atoms.

Fundamental characteristics of heat transport in atomic systems mean that the size of the system / number of atoms affect the magnitude of the conductivity result. Measures exist to quantify these effects, but simulations may yield incorrect results if system size is not considered. I will look into this to validate my calculated results, but also to offer analysis of these finite size effects (FSE) for atomic simulations in general.

!!! ADD REFS OBVS

1.2 Structure of the Earth

ENTIRE SECTION NEEDS FIGURE

The average radius of the Earth is 6371 km, the properties of which change dramatically with depth to the centre. I will be focussed on the lower mantle, particularly the region close to the core (the core mantle boundary, CMB). Events in the lower mantle influence (and are influenced by) the upper mantle and lithosphere above, and the core below. Heat transport throughout the Earth is influenced by thermal conductivity, which in turn affects the dynamics of the system, the surface expression of this being plate tectonics. Heat flow also affects the core geodynamo, which produces the Earth's magnetic field.

1.2.1 Lower mantle

!!! SiO₂ PHASES?

The lower mantle encompasses the region between the mantle transition zone (660 km deep, ~1900 K, ~25 GPa) and the CMB (2900 km deep, ~4000 K, ~136 GPa). The composition of this region can be approximated as 75% bridgmanite (MgSiO₃, magnesium silicate perovskite), 20% periclase (MgO, magnesium oxide), and 5% calcium silicate (CaSiO₃) perovskite (Trønnnes, 2009). All of which are insulators and past their Debye temperatures at lower mantle conditions, with the potential for the inclusion of impurities such as iron and aluminium.

The exact nature of impurities is complicated to resolve, as there are a lot of variables. Iron comes in ferrous and ferric varieties, which can have varying electron spin states. The amount of iron is not partitioned evenly throughout the mineral phases, periclase taking a larger proportion than bridgmanite for example. The nature of partitioning changes with physical conditions, where post-perovskite may behave differently to bridgmanite.

A popular opinion is that bridgmanite is stable in the lower mantle until the bottom few 100 km, where it undergoes a pressure-driven phase change to post-perovskite (Murakami et al., 2004; Oganov and Ono, 2004). In places, close proximity to the CMB might transform post-perovskite back to perovskite structure due to the increased temperature. This “double crossing” of the bridgmanite stability range can be imaged seismically, where lens-like bands of post-perovskite are shown to pinch out laterally (Lay et al., 2006).

The lower mantle is not heterogeneous, with large-scale features around the CMB. Two large low shear velocity provinces (LLSVPs) can be found roughly underneath Africa and the Pacific. An associated feature is the ultra-low velocity zones (ULVZs), identified around the edges of LLSVPs. These can be observed seismically, but the reason they exist is unclear. It is suggested they are “thermo-chemical features”, hotter and denser than the regular lower mantle. Increasing temperature and density tend to reduce seismic velocity, with increased density to offset the additional buoyancy from raised temperature. “Thermo” intuitively refers to the change in temperatures, while “chemical” changes are required to explain density increase. As a result, thermal conductivity will vary within these regions. Adding impurities such as iron would be a possible cause for density increase, such that the conductivity change should be quantified.

1.2.2 Above the lower mantle

The lithosphere (from 0 km depth) and upper mantle lie above the transition zone (to 660 km depth), which marks the top of the lower mantle. Although the chemistry of these regions is similar to that of the lower mantle, the physical conditions and mineral phases are different. Eruptive and subductive behaviour associated with

plate tectonics is perhaps the most obvious consequence of mantle dynamics at the Earth's surface, and generally to humanity.

The “rocky” portion of the Earth (from the surface down to CMB) is largely some form of silicate mineral, often with magnesium.

1.2.3 Below the lower mantle

The region beyond the CMB (starts at 2900 km depth) includes the core, comprised of its outer and inner sections. The liquid outer core extends to 5100 km depth, where the pressure-driven transition to solid inner core occurs. The composition of the core is dominated by iron, with various light elements suggested as possible alloying components.

Relative to the lower mantle, the outer core is a vigorously convecting system, and the core-side CMB can be considered to be an isothermal boundary. The main relevance to the lower mantle is the heat transfer across the CMB, the rate of which depends on the mantle conductivity and temperature. A second concern is that of chemical transfer between core and mantle, where iron from the core would be swapped various light mantle elements. Fe-content may increase in the lower mantle with CMB proximity, which in turn affects conductivity and the temperature profile for CMB heat flux.

1.3 Defining thermal conductivity

Thermal conductivity is a material property, indicative of the ease with which heat is transferred through conduction. For known substances thermal conductivity spans about six orders of magnitude, from silica aerogels with $0.005 \text{ Wm}^{-1}\text{K}^{-1}$ (Lee et al., 1995) to graphene with $5000 \text{ Wm}^{-1}\text{K}^{-1}$ (Balandin et al., 2008).

The transfer of thermal energy can occur between an object and its surroundings, two bodies brought into contact, or along a temperature gradient within an object. The possible mechanisms by which this can occur are conduction, convection, and radiation. Conduction is the transfer of heat by atomic vibrations, and electron transport in metallic substances (such as in the outer core). Convection is the motion of thermal energy via a moving medium, generally in liquids and gases (but expected

in the mantle). Density differences are the driving force for convection, due to the volume change associated with thermal expansion. Radiation refers to the transport of heat by electromagnetic radiation in the form of photons.

I am primarily concerned with the atomic vibrations of lattice conduction through the lower mantle, and secondly the convective behaviour therein. Mantle minerals are expected to be insulators, meaning there is no contribution from electron transport. The radiative component of thermal conductivity in the mantle is thought to be small (Goncharov et al., 2008), and will not be determined as part of this work. In the event that radiation contributes significantly to the effective thermal conductivity (Keppler et al., 2008), it can simply be added to the lattice component.

Convection in the mantle is dependent on the thermal conductivity, and will occur if heat cannot be sufficiently transported by conductive processes. The value of the Rayleigh number describes the behaviour of heat flow in a fluid, relative to a critical value for the system. Many variables are required to determine the Rayleigh number, but most importantly here it is inversely proportional to thermal conductivity. If the calculated Rayleigh number is lower than the critical value, conduction is the dominant process. When the Rayleigh number is greater, the ratio between it and the critical value describes the vigour and style of convection.

1.3.1 Mechanisms of heat transport

Electron

Close parallels exist between thermal and electrical conduction. The conduction of thermal energy in metals is predominantly due to the motion and interaction of free electrons. Heat is transferred as electrons move and collide in the lattice. There is no net transport of electrons in order to maintain charge neutrality within the lattice.

Photon

Any body with a non-absolute zero temperature emits thermal radiation as light, or photons. Radiative thermal conductivity is determined by a material's optical absorptivity, which describes how heat is transferred by electromagnetic radiation within a material. On the atomic scale, charged particles vibrate and emit light.

Energy is transferred from one particle to another when this light is scattered or absorbed. The transfer of heat by radiation is limited similarly to the transfer of visible light, with difficulty passing through opaque media. Unlike lattice conductivity at mantle conditions, radiative conductivity increases with temperature (Hofmeister, 1999). This relation has been used to assume thermal conductivity could be constant through the lower mantle if radiative processes are significant, where the lattice component decreases at the same rate the radiative increases (Tang et al., 2014).

Phonon

The final way heat is conducted is by the vibration of atoms, where the velocity of an atom is proportional to its heat. As an atom vibrates, forces act on neighbouring atoms, inducing motion. Hot atoms in a closed system transfer energy to cold atoms in this way, until energy and temperature are both equilibrated. Considering a crystalline arrangement of atoms, there is long-range structure and well-defined bonds between atoms. Much like standing waves on a string, atoms can vibrate in-phase. These patterns of vibrations are called phonons, and can be differentiated by wavelength and the relative motions of atoms.

Similar to the observed behaviour of photons, phonons exhibit wave-particle duality. This is necessary to describe how phonons interact with structural discontinuities and in a phonon-phonon collision. As a particle, a phonon is a quantised packet of vibrational energy. Unlike electronic heat conduction, there is a net motion of phonon “particles” from hot to cold regions, and the amount of active phonon modes increases with temperature. For a given material at constant conditions, there is a temperature at which thermal conductivity peaks. Up to this temperature, some phonon wavelengths are inactive in heat transport. Above this temperature, increased frequency of phonon-phonon collisions cause scattering, tending to reduce the efficiency of heat transfer. In the lower mantle, we are above this critical temperature for all physical pressure conditions, thus increasing temperature reduces conductivity.

1.3.2 What affects it?

pressure, temperature, and composition

temperature dependence from 0 K

pressure increase

refer to composition effects in chap 4

Heat is transported as lattice vibrations, or phonons. The further phonons travel before scattering (mean free path, MFP), the more efficient the heat transport and thus higher the thermal conductivity. A number of effects (MENTION MATTHIESSEN'S RULE) cause phonons to scatter: (1) collisions with other phonons in the lattice, (2) boundaries or defects in the material, and (3) impurities in the atomic structure.

1.4 Previous work - geophysics

1.4.1 STUFF THAT IS INFLUENCED BY CONDUCTIVITY

Thermal conductivity in the deep Earth influences dynamic processes such as mantle convection and heat loss from the core (Lay et al., 2008). In this section I will discuss the prominent thermal conductivity-dependent processes.

Mantle dynamics

In the lower mantle thermal conductivity changes with pressure, temperature, and composition, influencing features on a large scale. For example, Naliboff and Kellogg (2006) used numerical models of mantle convection to show size and stability of convective plumes are sensitive to thermal conductivity above the core mantle boundary (CMB).

Dubuffet and Yuen (2000) investigated the effects of temperature and pressure-dependent thermal conductivity on mantle convection, finding that depth-dependent thermal conductivity encouraged heat transport via convective plumes. Compared to a constant conductivity model, vertical heat transfer was concentrated to these "pipe-like" structures, despite the horizontally-averaged heat flow for both systems being around the same value. Variable conductivity, even in one dimension, increased the spatial and temporal stability of convection. Plumes were thicker, had heads of larger surface area, and were hotter, compared to the uniform conductivity mantle model.

Heat flow

The most accessible estimate of the Earth's energy is the total heat flow at the surface, of which a value of 46 ± 3 TW is accepted as the upper bound. Sources of surface heat flow include; radiogenic heating (20 ± 3 TW), mantle cooling (8–28 TW), and the conduction of heat across the CMB from core cooling (Lay et al., 2008). Conductive heat flow is constrained by thermal conductivity, a model of which is not available for all Earth conditions.

Better constraints on thermal conductivity are required to estimate CMB heat flow. This in turn would tell us more about the temperatures either side of the CMB, as well as the presence and nature of the lower mantle thermal boundary layer (TBL). Employing the most commonly used value for lower mantle conductivity, $10 \text{ Wm}^{-1}\text{K}^{-1}$ (Lay et al., 2008), heat flow across the CMB is expected to be 5–13 TW (Lay et al., 2008). The value of $10 \text{ Wm}^{-1}\text{K}^{-1}$ used by Lay et al. (2006) is an estimate of lowermost mantle thermal conductivity, based on extrapolation of a measurement at ambient conditions (Osako and Ito, 1991). Both higher and lower values have been proposed ($4\text{--}16 \text{ Wm}^{-1}\text{K}^{-1}$, Manthilake et al., 2011), illustrating how poorly constrained thermal conductivity is at CMB-relevant pressure/temperature conditions.

Geomagnetism

Using shear wave velocity as a proxy for CMB heat flow, Gubbins et al. (2007) showed that variations in mantle temperature gradients above the CMB can influence Earth's geodynamo. The present day magnetic field at the surface has four lobes, and these align above regions of fast shear wave velocity on the CMB. Ignoring compositional effects in the mantle, seismically-fast regions can be assumed to be cold. Considering Fourier's law (CITE), colder regions facilitate larger heat flows through steeper temperature gradients from the isothermal CMB.

Gubbins et al. (2007) recreate the geomagnetic observation of the aforementioned lobes using a core geodynamo simulation, where the upper boundary (CMB, lowermost mantle bottom) condition was a laterally varying heat flux. Knowing the

thermal conductivity, especially as it changes with temperature, would better constrain mantle boundary conditions used in this and similar core dynamics models (Ammann et al., 2014).

1.4.2 DETERMINATIONS OF TC FOR EARTH MATERIALS/CONDITIONS

A range of atomic scale simulation methods are available to determine the lattice thermal conductivity of materials. These are invaluable for calculating thermal conductivity at conditions of which experiments are difficult, i.e. the extreme conditions found in the Earth's lower mantle (pressures and temperatures up to 136 GPa and 4000 K at the core-mantle boundary).

Many studies assume lowermost mantle thermal conductivity to be $10 \text{ Wm}^{-1}\text{K}^{-1}$ (e.g. Lay et al., 2008), but uncertainty in the extrapolation of experimental results made at low pressures and temperatures gives a range of $4\text{--}16 \text{ Wm}^{-1}\text{K}^{-1}$ (Brown and McQueen, 1986; Osako and Ito, 1991; Hofmeister, 1999; Goncharov et al., 2009; Manthilake et al., 2011; Ohta et al., 2012). I give a review of experimental and computational determinations of conductivity for Earth-relevant conditions, where the Direct and Green-Kubo calculation methods are elaborated later on in Section REF (somewhere in chap2).

Experiments

There have been several computational studies to calculate the lattice thermal conductivity of bridgmanite at CMB conditions. Osako and Ito (1991) measured the lattice thermal conductivity of MgSiO_3 perovskite, using a modified Ångström method. They investigated a temperature range of 160–340 K at ambient pressure. At 300 K, a conductivity of $5.1 \text{ Wm}^{-1}\text{K}^{-1}$ was obtained. This value is similar to that reported for chemical and structural analogues, MgSiO_3 enstatite ($5.0 \text{ Wm}^{-1}\text{K}^{-1}$ REF) and CaTiO_3 perovskite ($4 \text{ Wm}^{-1}\text{K}^{-1}$ REF). The authors extrapolated the value to mantle conditions, neglecting radiative thermal conductivity. They predicted a value of $3.0 \text{ Wm}^{-1}\text{K}^{-1}$ just beneath the mantle transition zone at 1900 K, and $12.0 \text{ Wm}^{-1}\text{K}^{-1}$ at the top of the D'' layer at 2500 K, a four-fold increase. Thermal conductivity is highlighted as an important indicator of lowermost mantle structure, whether or not the D'' layer can behave as a thermal boundary between core and mantle.

Manthilake et al. (2011) measured MgSiO_3 perovskite at 26 GPa and 473–1073 K, and periclase at 8 and 14 GPa between 373–1273 K. In order to estimate values of thermal conductivity at the top and bottom of D'' for a lower mantle compositional model of 4 perovskite : 1 periclase, the authors extrapolated their measurements to high temperature and pressure. For an iron-free mantle, thermal conductivities of $18.9 \pm 1.6 \text{ Wm}^{-1}\text{K}^{-1}$ and $15.4 \pm 1.4 \text{ Wm}^{-1}\text{K}^{-1}$ are estimated for the top of D'' and CMB respectively. Similarly, for a mantle composition with Fe, thermal conductivities of $9.1 \pm 1.2 \text{ Wm}^{-1}\text{K}^{-1}$ and $8.4 \pm 1.2 \text{ Wm}^{-1}\text{K}^{-1}$ are calculated. This highlights the importance of impurities in controlling thermal conductivity in the lower mantle.

Ohta et al. (2012) measured the lattice thermal diffusivity of MgSiO_3 perovskite and post-perovskite at room temperature and pressures up to 144 GPa (using a diamond-anvil cell and light heating thermorefectance). These results suggest a majority perovskite lowermost mantle would have conductivity of $\sim 11 \text{ Wm}^{-1}\text{K}^{-1}$, and that parts of the lowermost mantle where post-perovskite is stable will have a conductivity approximately 60% higher. The authors suggest that these differences in conductivity between phases will not have a large effect on CMB heat flux, assuming the double-crossing perovskite phase model. The lattice conductivity of MgSiO_3 perovskite is shown to increase with pressure and decrease with temperature as expected. The inclusion of impurities is expected to decrease lattice thermal conductivity.

MANTHILAKE'S HIGH T RESULTS? CAN'T FIND REFERENCE?

Calculations

Haigis et al. (2012) used the Green-Kubo method (refer to REF) to calculate the lattice thermal conductivity of bridgmanite, post-perovskite, and periclase at lower mantle conditions. Assuming an iron-free composition with four parts bridgmanite to one part periclase, a model is constructed of density and temperature-dependent thermal conductivity along a geotherm. This model suggests great variation over the lower mantle, with a value of $9.5 \text{ Wm}^{-1}\text{K}^{-1}$ at the top and $20.5 \text{ Wm}^{-1}\text{K}^{-1}$ above D'' . Based on the results of Manthilake et al. (2011), Haigis et al. suggest the inclusion of iron will lower thermal conductivity by up to half, bringing their result in line with Lay et al. (2006) ($10 \text{ WMK}^{???}$). The authors estimate the CMB heat flux to

be 10.8 TW for an iron-bearing perovskite/periclase aggregate, dropping slightly to 10.6 TW for a similar post-perovskite aggregate. These values match other predictions of CMB heat flux (e.g. Lay et al., 2008).

Dekura et al. (2013) used *ab initio* anharmonic lattice dynamics with density functional theory (DFT) to calculate the lattice thermal conductivity of bridgmanite. At temperature of 300 K, they found conductivity increases from $9.8 \text{ Wm}^{-1}\text{K}^{-1}$ at 23.5 GPa to $43.6 \text{ Wm}^{-1}\text{K}^{-1}$ at 136 GPa. Temperature-dependence was found to be negative at 100 GPa, where conductivity decreases from $28.1 \text{ Wm}^{-1}\text{K}^{-1}$ at 300 K to $2.3 \text{ Wm}^{-1}\text{K}^{-1}$ at 4000 K. The pressure and temperature conditions used cover the entire range of accepted lower mantle conditions. From their results they calculated a Rayleigh number (Ra) of 10^5 – 10^7 for the mantle, in agreement with the geophysically-expected thermal convection (when $Ra < 10^3$ – 10^4). These results suggest that a CMB region at 136 GPa and 3200 K will have a conductivity of $5.3 \text{ Wm}^{-1}\text{K}^{-1}$, corresponding to a heat flux of 3–6 TW.

Ammann et al. (2014) used the direct method, a non-equilibrium molecular dynamics technique, to calculate the lattice thermal conductivity of bridgmanite and post-perovskite under D'' conditions. They found the conductivity of post-perovskite to be around 50% larger than bridgmanite for the same conditions ($12 \text{ Wm}^{-1}\text{K}^{-1}$ compared to $8.5 \text{ Wm}^{-1}\text{K}^{-1}$). This relation is true even in the TBL, where increases in temperature reduce lattice conductivity for all MgSiO_3 phases. An interesting result of their work is the observation of anisotropy for post-perovskite conductivity. This may lead to a feedback mechanism, influence the formation and stability of convective plume structures.

Ammann et al. also investigated the effects of impurities on conductivity, substituting magnesium with iron. They increase the mass of Mg atoms to resemble Fe, which tends to reduce conductivity. The lower mantle distribution of iron is not yet well-understood, specifically the partitioning between bridgmanite, post-perovskite, and periclase. Interestingly, the authors observed saturation in the conductivity reduction associated with atomic impurities, even for small Fe concentrations (see 1.1). Extrapolations of variable-composition experimental results must be applied carefully, increasing iron content past a certain point will not reduce conductivity any further.

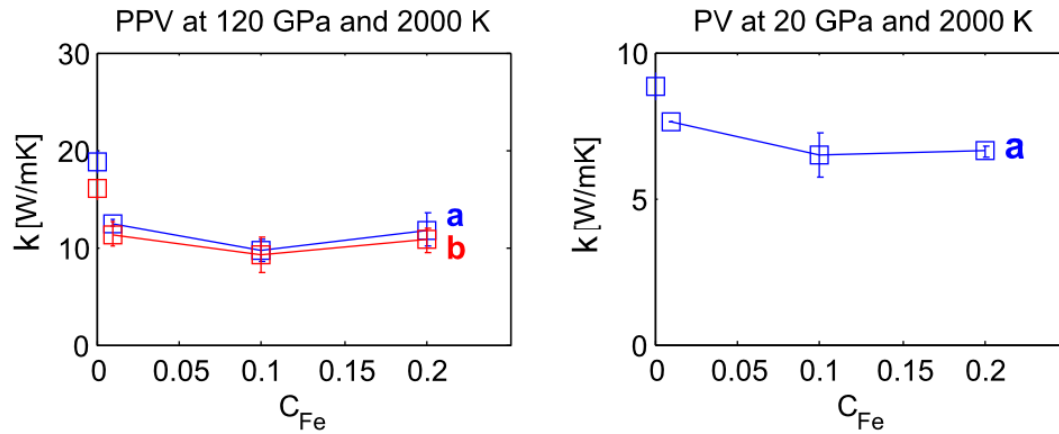


FIGURE 1.1: Thermal conductivity decrease due to inclusion of impurities is shown to saturate with increasing Fe-content, for $MgSiO_3$ post-perovskite and perovskite phases. **a** and **b** refer to crystallographic directions along which conductivity was calculated. Figure modified from Ammann et al. (2014).

Tang et al. (2014) performed first-principles calculations to assess the thermal conductivity of $MgSiO_3$ and the effect of Fe inclusions therein. These results feed into a model of conductivity along a lower mantle geotherm, of aggregate composition 4 bridgmanite: 1 periclase with 12.5% Fe impurities. Their calculations model $(Mg,Fe)SiO_3$ by increasing atomic mass, but not changing the force constants, in a manner similar to Ammann et al. (2014). The inclusion of impurities has little effect at 136 GPa-4000 K, on the order of a few percent, but they note MgO is affected more considering its higher conductivity. The observation that conductivity is reduced less when it is already small due to the effect of temperature, matches the saturation described in Ammann et al. (2014), but in turn disagrees with Haigis et al. (2012). The uncertainty is large when experimental data is extrapolated, especially when considering the (temperature-dependent) effect of impurities.

Radiative conductivity

Hofmeister (1999) produced a model of thermal conductivity for the entire mantle using data from infrared reflectivity methods. The radiative component at maximum was found to be small compared to the lattice conductivity, between 10–15% depending on the geotherm model used. This corresponds to radiative conductivity values of $0.67\text{--}0.82\text{ Wm}^{-1}\text{K}^{-1}$ compared to $5.8\text{--}6.7\text{ Wm}^{-1}\text{K}^{-1}$ for the total conductivity at the top of D'' .

Keppler et al. (2008) studied the near-infrared and optical absorption spectra of silicate perovskite up to pressures of 125 GPa at room temperature. From both their tests and visual inspection, it can be shown that their synthesised perovskite remains transparent at high pressures. Extrapolating their results to high temperatures (4500 K) they suggest that the maximum radiative thermal conductivity above the CMB is around $10 \text{ Wm}^{-1}\text{K}^{-1}$, implying that radiative conductivity is likely to be an important component of the total conductivity at lower mantle conditions. The study does not measure the variation of absorption spectra with temperature and pressure, of which experimentation is currently unfeasible.

Goncharov et al. (2008) performed a similar optical absorption spectra analysis up to 133 GPa, but with the opposite conclusion to Keppler et al. (2008). They agreed the radiative conductivity was dependent on the amount, redox state, and spin state of iron, but disagreed with its significance. Goncharov et al. (2008) estimated radiative conductivity would not exceed $0.54 \text{ Wm}^{-1}\text{K}^{-1}$ at the top of the D'' layer, a value in line with Hofmeister (1999) and at odds with Keppler et al. (2008). Until better constrained, it is convenient to assume the radiative component is small compared to the lattice component. As stated earlier (Section ??), the two components can simply be added to determine the total thermal conductivity (for the lower mantle).

Tang et al. (2014) re-evaluated the works of Keppler et al. (2008) and Goncharov et al. (2008) to create a profile of radiative conductivity in the lower mantle. Tang et al.'s profile suggests that the previous works have a more reasonable agreement than they show, using analysis which gives an upper bound on the conductivity. Radiative heat transfer is inhibited in the same way as conductive, by impurities and grain boundaries which are not considered when calculating this upper bound. Unlike lattice thermal conductivity, radiative conductivity increases with temperature, steeply so in the mantle thermal boundary layer. When the opposing temperature dependencies of lattice and radiative conductivity are considered in tandem, they suggest that the thermal conductivity of the lower mantle is largely temperature-independent above the D'' region at around $3 \text{ Wm}^{-1}\text{K}^{-1}$. Thermal conductivity increases to $5.5 \text{ Wm}^{-1}\text{K}^{-1}$ in the TBL, due to the increased significance of the radiative component.

1.5 Thesis outline

In Chapter 2 we provide an overview of the methods and expand on issues. I outline my computational approaches, for the non-equilibrium molecular dynamics direct method and equilibrium molecular dynamics Green-Kubo method. I show convergence of computed conductivity with respect to simulation cell size and shape

In Chapter 3, PRESSURE/TEMPERATURE EFFECTS. DISCUSS [P/T] SCALING LAW / THEORETICAL MODEL

In Chapter 4, ADAPTING SYSTEM TO INCLUDE IRON, DETERMINING EFFECT OF IMPURITY CONTENT, PRODUCING A MODEL OF THE LOWER MANTLE CONDUCTIVITY WITH VARIABLE TEMPERATURE AND BRIDGMANITE COMPOSITION

1.5.1 Aims

1.5.2 Objectives

Chapter 2

Intro/Background/Theory 2

2.1 Atomic-scale modelling

THIS IS JUST AWFUL

Knowledge of thermal conductivity is important for modelling the deep earth, but can not be measured experimentally at core mantle boundary conditions. Atomic scale simulations sidestep experimental limitations, but system size must be chosen carefully in order to determine accurate conductivity values.

Classical molecular dynamics approaches are utilised, with the intention of constraining appropriate system parameters. MOVE TO CLASSICAL POTENTIAL SECTION

A range of atomic scale simulation methods are available to determine the lattice thermal conductivity of materials. These are invaluable for calculating thermal conductivity at conditions of which experiments are difficult, e.g. the extreme conditions found in the Earth's lower mantle (pressures and temperatures up to 136 GPa and 4000 K at the core-mantle boundary).

2.1.1 Molecular dynamics

TRANSFER

Parameter drift/convergence

We ensure all calculations are run for a sufficient length of time for the conductivity value to converge. When conductivity fails to converge it means either the

simulations needs to be run for longer (unlikely with our nanosecond-scale classical calculations), or the system temperature has drifted. When NVE simulations are run for a long time there is noticeable drift in the average system temperature (due to numerical approximations in the equation of motion), which in turn causes drift in the computed conductivity.

NPT-NVT-NVE PROCESS

2.1.2 Interatomic potentials / Atomic interactions?

With the interatomic potential of Oganov et al. (2000) we simulate bridgmanite, a magnesium silicate otherwise referred to as MgSiO_3 or perovskite (the name of its crystal structure family). To assess finite-size effects we use larger simulation cells than those employed in previous studies. The atom counts associated with these cells (the largest cell considered having over 100,000 atoms) means an ab initio study would be impractical, necessitating the use of interatomic potentials. We expect the potentials to represent the finite size effects well, even if computed conductivities may inaccurate compared to first-principles calculations.

WHY OGANOV?

WHAT CUTOFFS?

TRANSFER

2.1.3 LAMMPS

LAMMPS (Large-scale Atomic/Molecular Massively Parallel Simulator) is a classical molecular dynamics code (Plimpton, 1995).

2.1.4 DFT/other

Required? Subsubsection somewhere?

2.2 Computing thermal conductivity

Stackhouse and Stixrude (2010) review different methods to compute thermal conductivity, in the present work we focus on two of these: (1) Equilibrium molecular

dynamics based on the Green-Kubo relations to determine the thermal conductivity from heat flux fluctuations and their time-dependence (Green, 1954; Kubo, 1957; Kubo, 1966; Schelling et al., 2002). (2) The non-equilibrium molecular dynamics-based “direct method”, where thermal conductivity is calculated from an imposed heat flux and corresponding temperature gradient via Fourier’s Law (Müller-Plathe, 1997; Nieto-Draghi and Avalos, 2013).

2.2.1 Finite-size effects

[[[Give its own section, or as subsection in each method?]]]

Computational techniques are not limited by the reproduction of physical conditions like experiments, however they are affected by the size and shape of the simulation cell. The effects of the finite system size available for computation must be checked, as systems with too few atoms are sometimes unable to reproduce the behaviour of the bulk material. If the wavelength of a phonon is too long to fit into a cell, it is not able to transport heat like it should. In the case of the direct method, the length to cross sectional area (CSA) aspect ratio can also matter.

Considering systems of varying size, length-dependent conductivities are obtained from the direct method and extrapolated to the bulk material (Schelling et al. (2002)). The validity of this extrapolation procedure have been called into question (e.g. Sellan et al. (2010)), when a linear trend cannot be fit through the length-dependent conductivities. We describe finite-size effects (FSE) which cause the conductivity result of a simulation to diverge from the value expected by a linear trend, and offer a comparison with results obtained from the Green-Kubo method. The two methods have previously been compared (e.g. Schelling et al. (2002) [[[REFERENCED EARLIER IN THIS PARAGRAPH, THIS OKAY?]]]), and have been found to give results in good agreement.

The finite-size effects (FSE) I describe are associated with phonon-phonon scattering, or the lack thereof, and boundary-scattering or truncation of phonon mean free path due to limited system sizes. These phenomena combine to misrepresent the phonon behaviour of the bulk material.

The FSE observed for a material change with thermal conductivity/phonon MFP,

and thus are pressure, temperature, and composition sensitive. Higher conductivity(or is it MFP?) materials/conditions require larger systems to eliminate FSE (and vice versa) [[[BUT IS THIS TRUE?]]].

2.2.2 Direct method

The direct method is the computational implementation of a typical experiment to measure thermal conductivity, using Fourier's law to relate heat flux (q) and temperature gradient (∇T) to thermal conductivity (k),

$$q = -k\nabla T. \quad (2.1)$$

System setup

In the direct method energy is transferred from one group of atoms to another, creating hot and cold regions between which heat flows. The resultant temperature gradient is measured by calculating the temperature of individual groups of atoms along the direction of the heat flux. Simulation cells tend to be long relative to their cross-sectional area, defined as height by width (see Figure 2.1). Cell boundaries are periodic and the hot and cold sections are half the cell length apart, meaning heat flows in both directions from hot to cold (one of which is across the length-end periodic boundary). This results in two similar temperature gradients which can be averaged.

From kinetic theory [[[REF?]]], conductivities computed by the direct method (k_L) are dependent on length of simulation cell,

$$k_L = \frac{1}{3}C_V v l_L, \quad (2.2)$$

where C_v is the volumetric heat capacity, v is the average phonon drift velocity, and l_L is the phonon mean free path.

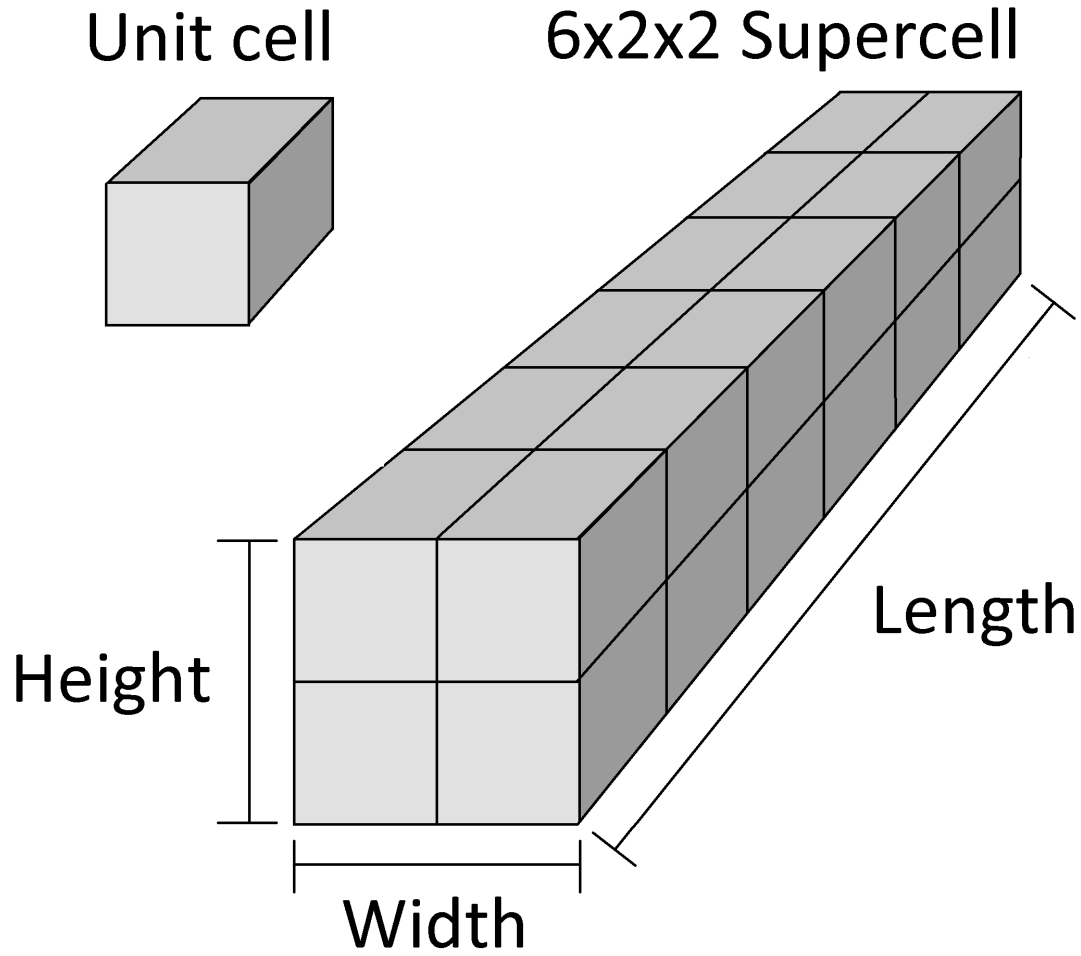


FIGURE 2.1: The unit cell represents the smallest box of atoms that can be replicated to produce a crystal structure. A supercell is an arrangement of unit cells.

Data processing

The finite size of the simulation cell truncates the mean free path, underestimating conductivity compared to that of the bulk material (k_∞). Using results from simulations of varying cell length (L), conductivity is extrapolated to a length-independent value (where b is a material dependent parameter),

$$k_L^{-1} = bL^{-1} + k_\infty^{-1}. \quad (2.3)$$

Inverse conductivities from direct method simulations are plotted against corresponding inverse cell lengths. A straight line is fit to the data and extrapolated to the y-axis (at which the inverse cell length equals zero and real length equals infinity), where the intercept gives the inverse of the bulk material conductivity (Schelling et

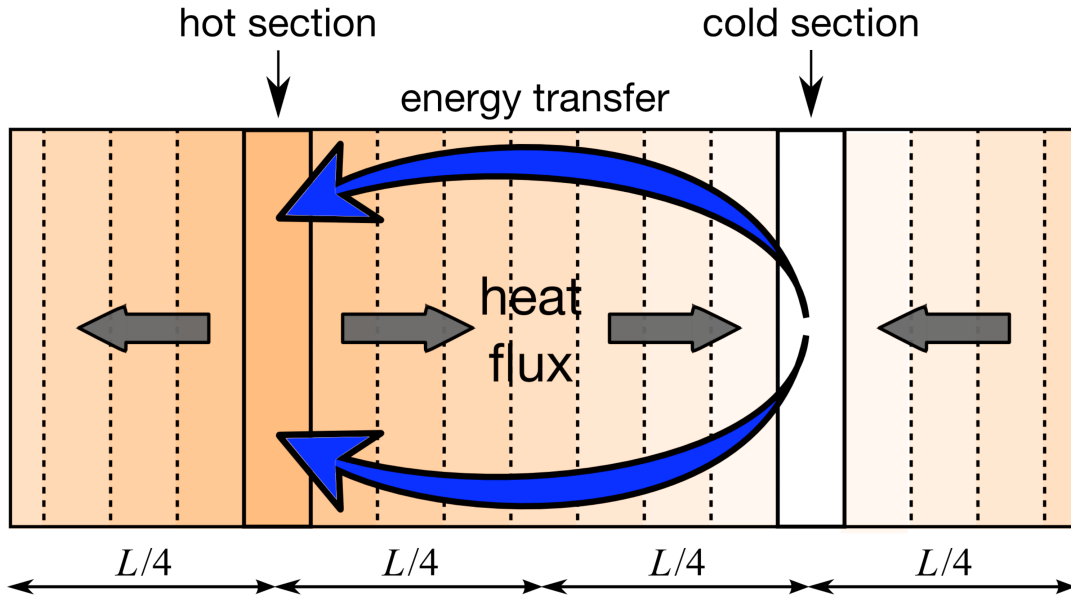


FIGURE 2.2: Movement and distribution of heat in the direct method. Orange to white scale represents temperature (modified from Stackhouse et al., 2015).

al., 2002).

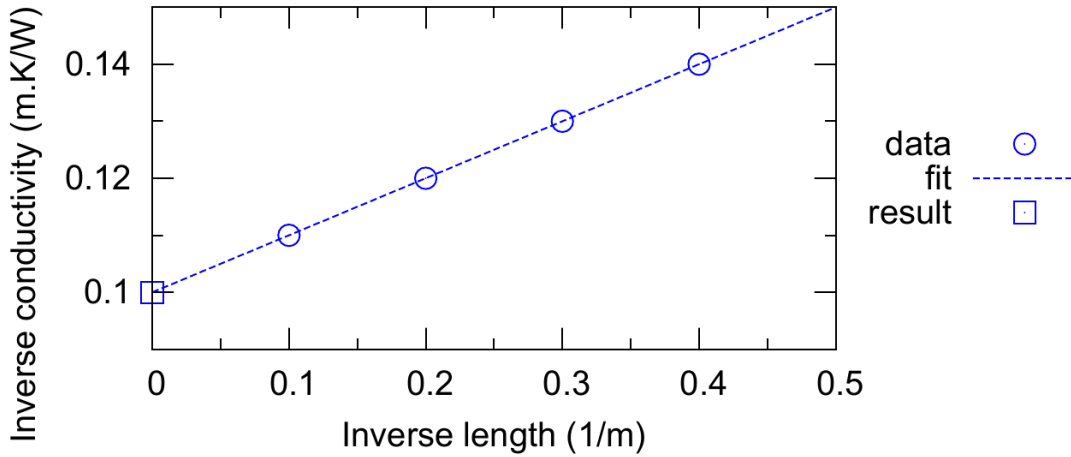


FIGURE 2.3: Idealised example of linear extrapolation procedure. Inverse computed conductivities are plotted against inverse simulation lengths. Extrapolation to y-axis gives conductivity of an infinite system length, i.e. the bulk material.

Finite-size effects

Problems arise when the data do not support a linear trend. There are two effects of finite system size that can cause an individual direct method simulation to diverge away from an inferred/expected linear trend, both of which result in overestimation of the length-dependent conductivity data point. First, when the distance between

hot and cold sections (controlled by cell length) is shorter than the MFP, phonons travel ballistically (i.e. without any scattering events) from heat source to sink (Sellan et al., 2010). Conductivities in shorter length cells are overestimated when this occurs, reducing the gradient of the linear fit and thus underestimating the extrapolated conductivity.

For a given length, conductivity is dependent on the CSA, or aspect ratio of the simulation cell. Conductivity is overestimated due to an underestimation of phonon-phonon scattering, from sparse phonon phase sampling in cells where cross-section is small compared to length. Phonons that aren't resolved cannot contribute to phonon-phonon scattering effects. Reduced scattering means heat transport is artificially more efficient than expected from the bulk material.

[[[SPECIFIC ALERT, REFERENCING THINGS I FOUND]]] However, the required CSA to abate this FSE is length-dependent. When the CSA is smaller than required for all cell lengths (e.g. 1x1 [FIGURE]), all conductivities are overestimated (Thomas et al., 2010, albeit for nanotube diameter?). As the CSA is increased, the data points (and thus also the extrapolated result) shift to lower conductivities (higher inverse conductivities). It is at this point that the short cells with lengths of similar order, will report conductivities converged with respect to CSA. Assuming these cells are sufficiently long to avoid the ballistic phonon transport (BPT), a linear fit can be extrapolated to obtain conductivity (for CSA around 2x2, the case at 4000 K).

The convergence is not necessarily observed concurrently for longer cells however, where they may show overestimated conductivities compared to the fit through short cells (Hu et al., 2011). This would cause the fit to all data to be steeper than it should, increasing the extrapolated result. [[[HOPEFULLY THIS IS TRUE]]] I can show that increasing CSA does not change the computed conductivity at short lengths, but does reduce values from longer cells and bring them into alignment with the expected fit.

Other NEMD

Fixed ends?

Sinusoidal temperature perturbation.

2.2.3 Green-Kubo

The Green-Kubo method uses auto-correlation functions (ACFs) to quantify time-dependence of heat fluxes (shown in Figure 2.4, and Equation 2.4), in a simulation cell of roughly cubic dimensions (WHY??) and spatially-consistent average temperature. Instantaneous heat fluxes can be used to determine how energy is dissipated within a system, where brief flux events mean heat is transferred quickly indicating high thermal conductivity [[[and vice versa, BUT IS THIS TRUE?]]].

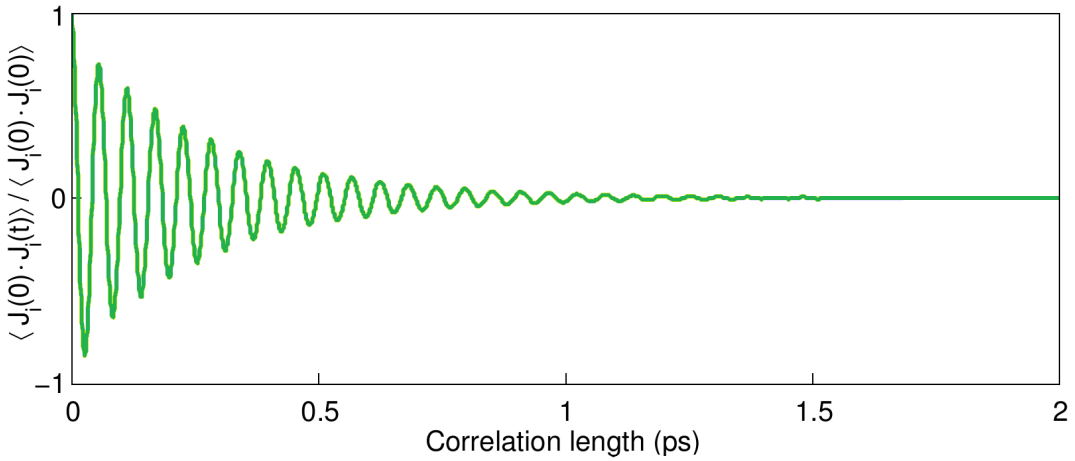


FIGURE 2.4: Normalised ACF. Correlation is taken over a longer length than shown on this plot (100 ps), however the function decays to less than 1% of its initial value at 2 ps. It continues to oscillate about zero, with a positive average value.

The auto-correlation is obtained over the net heat flux series in each crystallographic direction, for a timescale up to a chosen correlation length.

$$ACF_i = \langle J_i(0) \cdot J_i(t) \rangle, \quad (2.4)$$

where i specifies direction, J is heat flux, and t is the correlation length. The integral of heat flux ACF is proportional to thermal conductivity via the Green-Kubo equation (see Figure 2.5 and Equation 2.5),

$$\kappa_i = \frac{V}{k_B T^2} \int_0^\infty \langle J_i(0) \cdot J_i(t) \rangle dt, \quad (2.5)$$

[[[I am using “k”s and “kappa”s to represent thermal conductivity, kappa here and k earlier?]]] where V is the simulation cell volume, k_B is the Boltzmann constant, and T is the average temperature of the system. In this study we use Green-Kubo results

as an independent check on the direct method, as they do not have the same finite size-effects. Obtaining a converged conductivity result simply depends on using a large enough cell volume / number of atoms.

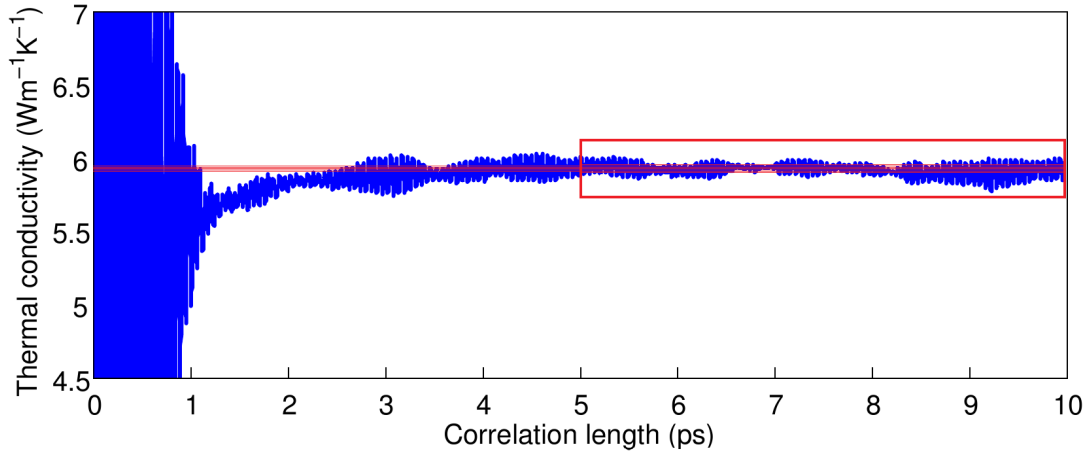


FIGURE 2.5: Integrated ACF, multiplied by constants to get thermal conductivity. Large variation in the first 1 ps corresponds to the correlation time where the ACF is unconverged (still decaying / large oscillations). Thermal conductivity is averaged from correlation time of 5 ps - 10 ps (region in red box).

The individual integrals obtained from the Green-Kubo show variation from the average combined integral on the order of the mean. Many simulations from different initial temperature conditions are required in order to ensure good sampling of conductivity, as well as ensuring the computation time for each is long enough for convergence. This makes Green-Kubo a computationally expensive method, especially for large systems.

The ACF should decay to zero as correlation time tends to infinity, however noise in the ACF prevents this. This will ultimately cause the integral to diverge/drift on long timescales. Howell (2012) fits a series of exponential decays to their ACF, forcing the expected decay to zero and subsequent (constant) integral convergence. This represents a significant improvement on the conductivity estimate at long correlation lengths, but is mostly similar with the un-fit integrals early in the correlation. (INTEGRAL DRIFT FIGURE, JUST THE ONE INTEGRAL FOR 100PS)

(STACKHOUSE 2010 REFERENCES Volz and Chen 2000; Sun and Murthy 2006)

2.2.4 Other

(3) Anharmonic lattice dynamics (Tang and Dong, 2009).

(4) Combined quasiharmonic lattice dynamics and molecular dynamics method (Koker, 2009).

2.3 Previous work

2.3.1 Method comparison

2.3.2 Finite-size effects

Should this section be interspersed into when FSE are mentioned in methods?

STUFF THAT MIGHT BE WRONG BECAUSE FSE?

Chapter 3

Constraining the finite-size effects of molecular dynamics methods to compute thermal conductivity

3.1 Introduction

Knowledge of the thermal conductivity of solids is key in a wide range of technological applications and for our understanding of natural systems. For example, in the Earth's lower mantle thermal conductivity controls the nature of planetary convection (Tosi et al., 2013), and the heat flux out of the core which powers the geotherm. Low thermal conductivities are required in thermoelectric materials, to maximise the efficiency of heat-electricity conversion (Snyder and Toberer, 2008).

A range of atomic scale simulation methods are available to determine the lattice thermal conductivity of materials. These are invaluable for calculating thermal conductivity at conditions of which experiments are difficult, e.g. the extreme conditions found in the Earth's lower mantle (pressures and temperatures up to 136 GPa and 4000 K at the core-mantle boundary).

(MOVE - to where though?) Many studies assume lowermost mantle thermal conductivity to be $10 \text{ W m}^{-1} \text{ K}^{-1}$ (e.g. Lay et al., 2008), but uncertainty in the extrapolation of results made at low pressures and temperatures gives a range of 4 - 16 $\text{W m}^{-1} \text{ K}^{-1}$ (Brown and McQueen, 1986; Osako and Ito, 1991; Hofmeister, 1999; Goncharov et al., 2009; Manthilake et al., 2011; Ohta et al., 2012).

3.1.1 Finite-size effects

THE PROBLEM OF FSE IN COMPUTATIONAL TECHNIQUES

EXACERBATED BY RANGE OF LOWER MANTLE CONDITIONS

The effect of FSE on conductivity results depends on the magnitude of conductivity/phonon MFP/physical conditions. At low kappa/low MFP/high T/ (my 4000 K), no BPT is observed, and short cells (>16 unit cells) can be used for extrapolation. In fact, short cells must be used to extrapolate, unless CSA considerations are made to ensure convergence of long cell results.

At high kappa/high MFP/low T (my 1000 K), BPT must be considered at the shorter cells (just 6?). Effectively there is a "sweet-spot", a window of cell lengths for a given CSA that produce consistently-converged results. Long cells outside of the window require a larger CSA, short cells outside show BPT. At 4000 K the lower limit of the window is smaller than the minimum cell length considered, and the upper limit is between 16-24 unit cells. For 1000 K the lower limit of the window moves inside the simulated cell length range around 6-8 unit cells (OR MORE?). The upper limit of the window appears to be larger than 96 unit cells, including all long cells up to this value produces an extrapolation in agreement with GK.

3.2 Computational approaches

In this section I talk about my specific approaches to applying the methods discussed in Chapter 2

3.2.1 Direct method

The simulation supercell is split into sections along its length, each half a unit cell wide. Two of these sections, half the supercell length apart, are designated as the heat source and heat sink. We measure (HOW?) the temperature in all sections to obtain the temperature gradient. Heat flows in both directions from the hot section because of cell periodicity [NEED DIRECT METHOD DIAGRAM BY THIS PARA], meaning there are two temperature gradients to average. Where L is supercell length in unit cells and $S (= 2L)$ gives the number of sections, we obtain $S/2 + 1$ temperature points to fit the gradient. Because the temperature gradient is non-linear around the

heat source and sink, we ignore $S/12$ sections (rounded to nearest integer) from both ends of the temperature gradient. For a given simulation cell we fit $S/3 + 1$ points to obtain the temperature gradient. We use a minimum supercell length of 6 unit cells (12 sections, 5 data points), in order for sufficient fitting of the temperature gradient. [HOW NECESSARY IS THIS PARA, VERY JARGONY]

(MOVE TO RESULTS?) Changing the width of the heated sections has no effect on the conductivity result. Furthermore, changing the width (and thus number) of temperature bins has no effect on the sampled gradient, assuming resolution is large enough to capture the non-linear region around the heat source/sink.

An important factor for utilising the direct method is maintaining a sensible temperature gradient where Fourier's law remains valid, i.e. conductivity is constant along the length of the cell. Thermal conductivity is strongly temperature-dependent at upper lower-mantle conditions (1000 K), it is therefore undesirable to have substantially different conductivities as a function of temperature across the cell. The opposite case is also true, the difference in temperature between hot and cold sections must be larger than the uncertainty in the average system temperature.

We typically observe fluctuations in temperature of around ± 50 K during temperature equilibration, and look for temperature increases/decreases on the order of 10% the mean temperature. We control the magnitude of the gradient by altering the interval at which heat is exchanged. To produce the desired gradients we find shorter intervals are required as cell length decreases, cross-sectional area increases, and system equilibrium temperature decreases.

3.2.2 Green-Kubo

The bridgmanite unit cell does not have cell dimensions resembling a cube ($a:b:c = 1:1:1.4$), so we use supercell structures of $3 \times 3 \times 2$, $4 \times 4 \times 3$, $5 \times 5 \times 4$, $6 \times 6 \times 4$ etc. to make an approximately cubic simulation cell. Temperature initialisation (NVT) of 1 ns is run to ensure convergence of system pressure and temperature. To obtain heat flux auto-correlation functions, a simulation for each initial temperature condition is run for X ns, with 9 successive repeats for a total of 10 jobs. This gives 10 ACFs from

each initial condition. Simulation runs are split in this manner to be feasible computationally, and also to provide enough samples for ensemble averaging statistics (??).

3x3x2 - X = 10 ns, for 20 initial conditions - 2 μ s total time

4x4x3 - X = 10 ns, for 30 initial conditions - 3 μ s total time

5x5x4 - X = 5 ns, for 20 initial conditions - 1 μ s, X = 1 ns, for 70 initial conditions - 0.7 μ s, 1.7 μ s total time

6x6x4 - X = 1 ns, for 80 initial conditions - 0.8 μ s total time

THIS INFO IN A TABLE, OR JUST GIVE FOR THE RELEVANT VOLUME?

I DON'T LIKE THE INCLUSION OF ALL THE ABOVE INFORMATION

In this study we compute ACFs up to correlation lengths of 100 ps, with (100,000) 1 fs timesteps. This length is longer than required but selected as a proof of concept to show convergence in the conductivity result, additionally to display the extent and behaviour of drift in the integrals for long correlation times. We show in Figure ?? that the magnitude of the ACF decays to much less than 1% of its initial value around a correlation time of 1 ps, inferring the start of convergence for the integral and thus conductivity. (ACF FIGURE FOR CORREL < 10PS?, RUNNING AVERAGE SHOWS CONVERGENCE)

ACFs produced by each simulation are integrated separately, and averaged into a single series. This process is performed for heat fluxes in each crystallographic direction, to allow analysis of anisotropy and finite system size effects. From this combined integral we pick a window of correlation lengths to capture a flat, converged region (or the section just after the 'bottleneck' if convergence is not obvious). This correlation length window is then applied to all N integrals constituent to the combined series, giving N integral averages and corresponding standard deviations. A weighted average is then taken of these data points, to give a single value with uncertainty. This value is directly proportional to thermal conductivity, as given by EQUATION XXX.

Considering bridgemanite at lower mantle conditions, we find correlation time windows in the range of 2-30 ps to be suitable. At the low-end, this allows the initial high-variability in integral value to be ignored. At the high-end, the time is long enough for good sampling of the integral, but short enough to ignore the

drift-effects. The magnitude and range of the window typically increases with conductivity (or with decreasing temperature etc.), e.g. 2-10 ps at 4000 K, and 10-30 ps at 1000 K.

3.3 Results

3.3.1 Green-Kubo

A supercell volume of $3 \times 3 \times 2$ (((REFER TO GRAPH, WILL NEED 1000K TOO))) fails to reproduce conductivities on the same order as the larger cells for all directions. We identify $4 \times 4 \times 3$ and larger cells as being converged with respect to cell volume (((PROBLEMATIC STATEMENT, NOT CONVINCING, BY WHAT METRIC?))). This a useful result in terms of computation efficiency, as $6 \times 6 \times 4$ supercells are 3 times as large (VOLUMOUS? REFERENCE ATOM COUNT?) as $4 \times 4 \times 3$.

3.3.2 Direct method

When determining finite-size effects, it is important to consider the scenario with largest phonon mean-free paths. Phonon MFPs are largest at low temperatures (beyond the Debye temperature) and high pressures. In light of this we consider pressure of 136 GPa and temperatures of 1000 K and 4000 K. 136 GPa / 4000 K represents the expected conditions of the core-mantle boundary, whereas 136 GPa / 1000 K is unphysical in the context of the Earth but maximises MFP. UPDATE - GK RUINS EVERYTHING

By computing conductivities across a range of cell lengths we show that direct method simulations with small cross-sectional areas fail to produce converged results with respect to larger CSAs. Without considering any extrapolation, it is clear that small CSA cells overestimate conductivity (Figures ?? & ??) at conditions of both 1000 K and 4000 K. On both figures the results for cells with CSA 2×2 and larger plot close to on top of each other. Producing the same results as 8×8 cells, we conclude that cells with CSA of 2×2 are suitable for direct method simulations of bridgmanite.

Now considering CSAs of 2×2 , we examine the divergence of conductivity result with cell length from an expected linear trend (Figure ??). As mentioned in Section ??, cells that are too long or short cause a conductivity result to be overestimated. At

4000 K we find that cells up to 24 unit cells length (<0.06 in inverse length) produce a reasonably linear trend. At this condition, there is no reasonable overestimation due to short cells and ballistic phonon transport. However at 1000 K where the MFP is longer, a cell of length 6 unit cells (inverse length 0.167) produces conductivity larger than expected. The same long-cell divergence is found >24 unit cells length, the onset of insufficient phonon sampling. For all direct method simulations of bridgmanite at lower mantle conditions, we recommend employing cell lengths of 8 - <24 unit cells. Due to the increasing computational cost associated with cell length (especially for ab initio methods), we recommend the longest cells be 16 unit cells. FINITE SIZE EFFECTS INCREASE WITH MFP/KAPPA

Now we consider CSA of 2x2 and supercell lengths of 8, 10, 12, and 16 unit cells for comparison with the results from Green-Kubo. After performing a weight least squares regression (extrapolation) on the direct method results, we obtain a conductivity with uncertainty. Figure ?? shows the extrapolation and Green-Kubo result (at $x = 0$). They agree within error, meaning we have chosen a suitable set of criteria for working with direct method results. DO I NEED TO PROVE THAT OTHER LENGTHS/EXTRAPOLATIONS DON'T MATCH GK? FINE AT HIGH T / SHORT MFP, LOW T / HIGH MFP NEEDS LONGER CELLS TO EXTRAPOLATE, OR MORE SHORTER CELLS IGNORED.

3.4 Summary

For bridgmanite (at conditions representing the lower mantle), we show that use of the direct method for calculation of thermal conductivity will lead to an overestimate if the simulation cell is too long (>16 unit cells, 4000 ONLY!!!). Small cross-sectional areas ($<2 \times 2$ unit cells) also overestimate the thermal conductivity. This informs future work using Density Functional Theory, and will allow a model of lower mantle conductivity considering composition to be established [[[OOPS]]].

(ASSUMING THE RESULTS ARE CORRECT AND AGREE WITH GK) We see the non-linear region as described by Sellan et al. (2010) for the cell length of 6 unit cells at 1000 K, which has individually higher conductivity than expected from the

linear fit through data points corresponding to lengths of 8-16 unit cells. When included in the extrapolation, this reduces the gradient of the fit, raising the intercept and thus causing conductivity to be underestimated. At temperature of 4000 K, the 6 length cell is inline with the fit through other cells with length less than 16 unit cells. As the ratio of cell length to phonon MFP increases with temperature, we believe the onset of divergence as described by Sellan et al. moves to the right (??? - MENTION ACTUAL EFFECT - QUANTIFY RATHER THAN REFERENCING GRAPH). A shorter MFP needs shorter cell lengths to display divergent conductivity, of which we have not sampled (at high temperature). DOING THE DIRECT METHOD WITH CELLS OF LENGTH LESS THAN 6 UNIT CELLS AT ANY TEMPERATURE IS A BAD IDEA BECAUSE ...

We find conductivity is definitely dependent on CSA, but we were not able to increase CSA enough to eliminate aspect ratio-dependent divergence as reported by Hu et al. (2011). This does support our conclusion ignoring long cell lengths however, in order to keep the aspect ratio within a reasonable limit and ensure a linear fit is extrapolated. (EVEN THOUGH 48x8x8 HAS A SMALLER RATIO than 8x2x2?)

(WAFFLE ALERT) Ignoring the specifics of this study, we stress the importance of performing finite-size analysis when performing direct method calculations. Direct method cells spanning a range of lengths must be considered to find the linear regime for extrapolation. Cross-sectional area must be increased until the conductivity result converges. The same can be said about the Green–Kubo method, where the result converges with increasing volume. These effects vary with phonon mean-free path, sensitive to pressure, temperature, and compositional variations such as impurities. Completing finite-size effect analysis at conditions with the largest phonon mean-free path / thermal conductivity ensure all other conditions represent converged results. We believe classical molecular dynamics with interatomic potentials to be an excellent way of quantifying these effects quickly, performing ab initio methods (SHOULD I TAKE THIS SENTENCE OUT, NO PROOF OF THIS CLAIM).

Chapter 4

Modelling the thermal conductivity of Fe-bearing bridgmanite at the CMB

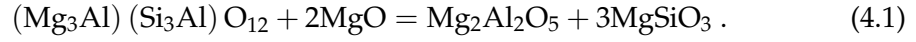
As stated earlier (REF), there are no experiments that can reach the high pressures and temperatures necessary to replicate the conditions of the lower mantle. The addition of impurities into minerals further complicates the matter. In addition to pressure and temperature-dependence, composition must be considered for full evaluation.

DISCUSS/RE-ITERATE EARLIER-DISCUSSED SEMI-RELEVANT EXPERIMENTS HERE, MANTHILAKE

4.1 Simulating the effect of atomic impurities

The bulk of the lower mantle comprises bridgmanite (~70%, and its high-pressure polymorph post-perovskite), ferropericlase (~20%), along with others (~10%) such as calcium silicate perovskite CaSiO_3 (Trønnes, 2009). The composition can vary within these mineral archetypes, significantly the concentration of iron impurities. Magnesium is replaced with iron in MgSiO_3 and MgO compositions, leading to FeSiO_3 and FeO endmembers. Aluminium can similarly be substituted for Magnesium and Silicon (as in Brodholt, 2000) where, ((DOES THIS NEED TO BE IN, WITH

AN EQ NUMBER?))



Impurities reduce thermal conductivity by providing more opportunities for phonon scattering events. An impurity is an irregularity to a propagating phonon, much like a speedbump to a car. They have different properties to the atoms the phonon expects to meet from crystal regularity, namely mass and their bonds with neighbouring atoms. For this reason that the thermal conductivity of a solid solution is lower at intermediate compositions than at the endmembers. Even if one endmember has lower conductivity than the other, an irregular mix of the two can produce even lower values.

4.1.1 How do impurities affect conductivity?

The effect of impurities on lattice thermal conductivity is approximated by Klemens (1960) and Padture and Klemens (1997), a review of which can be found in the Supplementary Material of Stackhouse et al. (2015). Equations hereafter in this section with a SS-prefix refer to their position in this supplementary material. The lattice thermal conductivity of a binary solid solution is given (Eq. SS6) as

$$\kappa_{\text{SS}} = \kappa_{\text{V}} \left(\frac{\omega_0}{\omega_{\text{D}}} \right) \arctan \left(\frac{\omega_{\text{D}}}{\omega_0} \right), \quad (4.2)$$

where ω_0 is the phonon frequency at which the mean free path is equal to that of the solute atoms, and ω_{D} is the phonon frequency corresponding to the maximum of the acoustic branch in the phonon spectrum (the Debye frequency). κ_{V} is the compositionally-weighted (Voigt) average of endmember conductivities,

$$\kappa_{\text{V}} = (1 - C) \kappa_1 + C \kappa_2, \quad (4.3)$$

where κ_1 and κ_2 are the solid solution endmember conductivities, and C is the fractional concentration of the second endmember (Eq. SS7).

ω_0/ω_D overview

When $\omega_0 \gg \omega_D$, $\arctan(\omega_D/\omega_0) \rightarrow (\omega_D/\omega_0)$, so $k_{SS} \rightarrow k_V$, the conductivity including the effect of impurities tends toward the endmember linear average. This is the scenario when other factors, such as Umklapp processes at high temperatures, have caused conductivity to decrease significantly. Adding impurities at this point has little additional effect, conductivity is already close to its saturated minimum.

On the other hand, when $\omega_D \gg \omega_0$, $\arctan(\omega_D/\omega_0) \rightarrow \pi/2$, but $(\omega_0/\omega_D) \ll 2/\pi$, so $k_{SS} < k_V$, and impurity scattering has a noticeable effect on the resultant conductivity. Adding impurities affects conductivity in this fashion when phonon-phonon collisions are not the dominant conductivity reducing process, like at low temperatures compared to the conditions mentioned in the above case. Additional information on ω_0 will be given at the end of this subsection.

What effects the magnitude of impurity scattering?

That factors that affect the severity of impurity scattering are temperature, the mass difference between the impurity and what it replaced, and the concentration of said replacements. The ratio of the phonon frequencies in Eq. 4.2 can be expressed (Eq. S11) as

$$\left(\frac{\omega_0}{\omega_D}\right)^2 = \frac{1}{(6\pi^2)^{1/3}} \frac{T}{3\varepsilon T_0}, \quad (4.4)$$

where T is temperature, T_0 is the temperature associated with ω_0 , and ε is related to the mass difference and proportion of endmembers by

$$\varepsilon = \frac{(M_2 - M_1)^2}{\bar{M}^2} C (1 - C), \quad (4.5)$$

where M_i is the atomic mass of the i -th endmember, \bar{M} is the mean atomic mass of the solid solution, and C is the proportion of endmembers (Eq. SS9).

As the temperature increases, so too does the left-hand side of Equation 4.4. As discussed earlier, this reduces the effect of scattering caused by impurities, which will be relevant at CMB conditions where temperature is large (~ 4000 K).

ε increases with the mass difference of the endmembers, and the impurity concentration. Increasing ε tends to reduce the phonon frequency ratio, meaning impurity scattering will affect the resultant conductivity more. The atomic masses of Mg and Fe are 24 and 56, so FeSiO_3 is 1.32 times heavier than MgSiO_3 .

As an aside, Equation 4.5 predicts that isotopic variations will have little effect on conductivity, where the mass changes are typically small (e.g. ^{24}Mg to $^{25/26}\text{Mg}$) and abundances are low (Mg standard atomic weight is 24.3, the ratio of ^{24}Mg to heavier isotopes is roughly 4:1). Mass difference is an additional reason why Fe impurities are more interesting theoretically than Al. The mass of Al is 27, compared to Mg with 24 and Si at 28.

The composition control term in Equation 4.5, $C(1 - C)$, increases from 0 to 0.25, when $x = 0.5$. ε increases with composition up to 50%, the furthest point away from both endmembers, therefore the condition of most disorder in the model. While I investigate the full range of C , most of the lower mantle $(\text{Mg,Fe})\text{SiO}_3$ is going to have compositions up to 20% Fe ((REF)). Knowledge of conductivity up to FeSiO_3 composition is interesting if ultra low velocity zones are thermochemical features of high Fe content (e.g. Mao et al., 2004; Dobson and Brodholt, 2005).

!!! MANTLE COMPOSITION REFERENCE NEEDED ABOVE

4.1.2 ω and τ in depth

ω_0 is defined (by Klemens, 1960, Eq. 11) as the frequency at which

$$\tau'(\omega_0) = \tau_u(\omega_0), \quad (4.6)$$

where τ' and τ_u are the contributions of point defect scattering and Umklapp processes respectively to the effective phonon relaxation time (Klemens, 1960, Eq. 2 & 3), where

$$1/\tau' = A\omega^4, \quad (4.7)$$

and

$$1/\tau_u = B\omega^2. \quad (4.8)$$

The effective phonon relaxation time of the system, using the Matthiesen Rule (modified from Klemens, 1960, Eq. 7), is

$$\frac{1}{\tau(\omega)} = \frac{1}{\tau_u} + \frac{1}{\tau'} . \quad (4.9)$$

When Equation 4.6 is satisfied, the effective relaxation time will equal to half of either its constituents,

$$\frac{1}{\tau(\omega_0)} = \frac{1}{\tau_u} + \frac{1}{\tau'} = \frac{1}{\tau_{\omega_0}} + \frac{1}{\tau_{\omega_0}} = \frac{2}{\tau_{\omega_0}} . \quad (4.10)$$

When $\tau' \neq \tau_u$, the effective relaxation time will tend toward the smaller of the two as the difference increases. I illustrate in Figure 4.1 that a process' relaxation time will dominate the other in the effective behaviour when it is around 1,000 times smaller. At the point where the contribution is equal (i.e. 0.5), the ω_0 criterion is satisfied (Eq. 4.6). The contribution varies linearly when the magnitudes of the relaxation times are comparable, adopting an arctan-like form when they vary greatly.

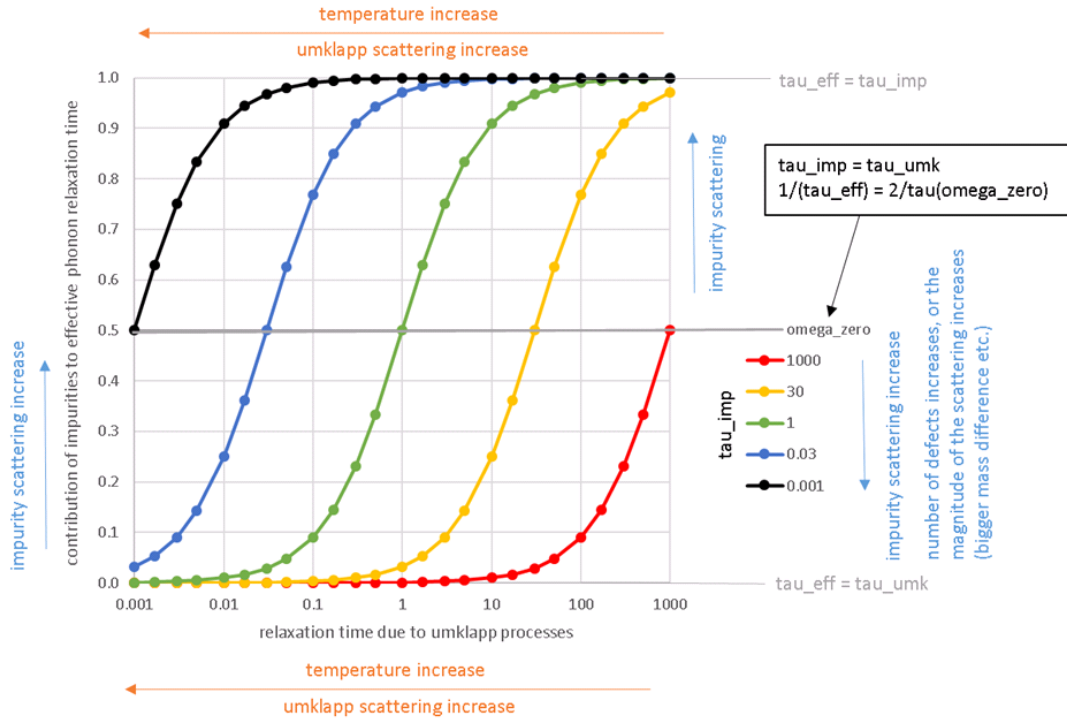


FIGURE 4.1: For a series of τ' , their contribution to the effective phonon relaxation time is plotted against τ_u . The quantity on the y-axis is the normalised difference in effective phonon relaxation time, comparing just Umklapp processes to Umklapp and the impurity scattering effect (as in Eq. 4.9).

For a CMB-like condition of high temperature, Umklapp process relaxation time

is short (left hand side of Fig. 4.1). Adding impurities (reducing τ') doesn't contribute much to an already large scattering effect. Where the Umklapp process relaxation time is longer (temperatures decreasing towards Debye temperature), even adding a small amount of atomic impurity can influence the effective system behaviour. Considering the average phonon velocity, a longer relaxation time means a greater distance travelled, or phonon mean free path.

Calling back to Equation 4.7 & 4.8, A and B are constants, where only the latter is temperature-dependent (T). The contribution of point defect scattering to the effective phonon relaxation time is constant with temperature (varying with impurity concentration and composition). It is the relative magnitude of τ_u , which decreases with temperature ($\propto 1/T$, via B), to τ' that influences the effect of impurities on thermal conductivity (see Equation 4.9).

The two relaxation time terms above can be equated via Equation 4.6, showing ω_0 is similarly temperature-dependent

$$\begin{aligned} A\omega_0^4 &= B(T)\omega_0^2, \\ \omega_0^2 &= B(T)/A, \\ \omega_0 &\propto T. \end{aligned} \tag{4.11}$$

The Debye frequency is a constant, so

$$\left(\frac{\omega_0}{\omega_D}\right) \propto T. \tag{4.12}$$

As temperature increases (above the Debye temperature), conductivity decreases because of Umklapp processes. The significance of point defect scattering (but not the magnitude of its relaxation time) decreases as the effect of phonon-phonon scattering increases. Therefore the relative conductivity decrease due to impurities is inversely proportional with temperature, and less important as conductivity tends towards its saturated minimum.

4.2 Methodology

In this section I outline the process of taking Fe from chemistry to computer, by fitting my own coefficients to a Buckingham potential. I also go over how the Fe is incorporated into the MgSiO_3 , considering its placement and concentration.

4.2.1 How does iron behave?

ELECTRONIC THERMAL CONDUCTIVITY???

I use two methods to introduce iron impurities to my bridgmanite models. The first approach is to simply create a magnesium atom with the mass of an iron atom, without changing any coefficients of the interatomic potentials from Oganov et al. (2000). Despite being an obviously "quick and dirty" method, (I will show) this is a reasonable first-order approximation(((PROVE IT!))). As the variation in mass number from Mg to Fe is large (24 to 56, a 133% increase), it is likely to change the behaviour of the system more than a subtle change in the atomic interactions.

MENTION MORE AMMANN IRON STUFF HERE, QUANTIFY/DATA? Approximating Fe with heavier Mg atoms is used by Ammann et al. (2014) to investigate $(\text{Mg,Fe})\text{SiO}_3$ with 20% impurity content at 20 GPa and 2000 K. They found the effect of adding impurities in this manner was variable on a number of factors (crystallographic direction, interatomic potential), and observed saturation in the conductivity decrease with concentration.

The second approach to add Fe into the MgSiO_3 system is to fit interatomic potentials, as well as using the aforementioned mass change for a more realistic model. I adapted the Oganov et al. (2000) MgSiO_3 Buckingham interatomic potential (U) to include the Fe-O interaction (see Table 4.1). I determined two short-range potential parameters, b and ρ , shown in Eq. 11 from Oganov et al. (2000),

$$U_{ij}(R_{ij}) = \frac{z_i z_j}{R_{ij}} + b_{ij} \exp\left(-\frac{R_{ij}}{\rho_{ij}}\right) - \frac{c_{ij}}{R_{ij}^6}, \quad (4.13)$$

where ij refers to an atom pair, R is interatomic distance, z is atomic charge, and c relates to the Van der Waals force (zero for non O-O interactions). We determine ρ in the same fashion as Oganov et al. (2000), calculated from the atomic first ionisation

potentials,

$$\rho_{ij} = \frac{1.85}{\sqrt{I_i} + \sqrt{I_j}}. \quad (4.14)$$

b is constrained using the GULP code (Gale, 1997), using the calculated ρ value for Fe-O. We fit to structural information from Parise and Wang (1990), an experimental study of $(\text{Mg}_{0.9}, \text{Fe}_{0.1})\text{SiO}_3$ bridgmanite at ambient conditions. This study was chosen as it matches the conditions at which Oganov et al. (2000) fit their potential.

TABLE 4.1: Parameters used to define Oganov et al. (2000)’s MgSiO_3 perovskite potential, including my fit Fe-O values.

Bond ij	b_{ij} (eV)	ρ_{ij} (Å)	c_{ij} (eV.Å ⁶)
Mg-O	1041.435	0.2866	0
Si-O	1137.028	0.2827	0
O-O	2023.800	0.2674	13.83
Fe-O	1440.437	0.2846	0

Despite potential fitting being an improvement on solely changing atomic mass, it is not perfect as I do not vary atomic charge from Mg to Fe. The problem is additionally complicated by the Fe-partitioning between MgSiO_3 and MgO , the effect of ferrous vs. ferric iron, and how spin state affects properties such as conductivity as it varies along the geotherm (((REFS?))). These additional complexities are beyond the scope of this project, where only ferrous iron will be considered. The effects of impurities (i.e. some kind of irregular atom) is interesting, even if the exact chemistry is not accurate.

!!! Validate potentials

!!! Validate Fe vs. heavy Mg, isotope mass

4.2.2 Where do the impurities go?

Iron is substituted with magnesium into the bridgmanite atomic structure. The unit cell contains 4 Mg atoms, and the smallest direct method cell I employ is a 6x2x2 supercell. Therefore the smallest amount of iron that can be added is 1/96 atoms, a concentration just over 1%. A simple MATLAB script (((APPENDIX/ONLINE?))) is used to modify LAMMPS input files, randomly selecting a specified proportion of Mg atoms to be replaced with Fe. When a Mg atom changes to Fe, its mass and interatomic potential properties change.

Due to the microscopic nature of the system, we do not want all of the added iron to be concentrated together in the simulation cell, especially in a heat source/sink region. To avoid this we order Mg atoms by length along supercell, and change a single atom every so many. For example, changing 1/4 atoms is different to changing 24/96. The latter has a higher variance in Fe per unit length, and the former chooses one atom to swap for every four along the system. These distributions are illustrated in Figure 4.2. After iron is added, the standard direct method or Green-Kubo workflow is followed.

4.3 Results

Lattice thermal conductivities obtained from Green-Kubo calculations are plotted against temperature in Figure 4.3, for Mg and Fe-endmembers and the 50/50 solid solution mix.

Conductivity decreases with temperature, approximately following $\kappa \propto 1/T^{0.9}$ at the pressure of 136 GPa considered here. This is in contrast to the typically expected $\kappa \propto 1/T$ relation, indicating some kind of saturation in conductivity decrease with temperature.

FeSiO₃ has a consistently lower conductivity than MgSiO₃, although both species may converge given a high enough, albeit unphysical, lower mantle temperature. This suggests there is a minimum conductivity associated with the crystal structure, reached first by FeSiO₃ with its inherently lower conductivity.

The 50% solid solution has a consistently lower conductivity than MgSiO₃, and a lower than or equal to relation to FeSiO₃. This is again to be expected, conductivity decreases from endmember to intermediate compositions as impurity concentration increases. It can be seen that conductivity differences are very small at high temperatures for FeSiO₃ and the solid solution. If FeSiO₃ has already reached its theoretical minimum, adding impurities will do little to decrease it further.

An alternative perspective to Figure 4.3 is presented in Figure 4.4, where Green-Kubo conductivity results are plotted as a function of Fe impurity content for several temperature series. Conductivity generally decreases with increasing temperature

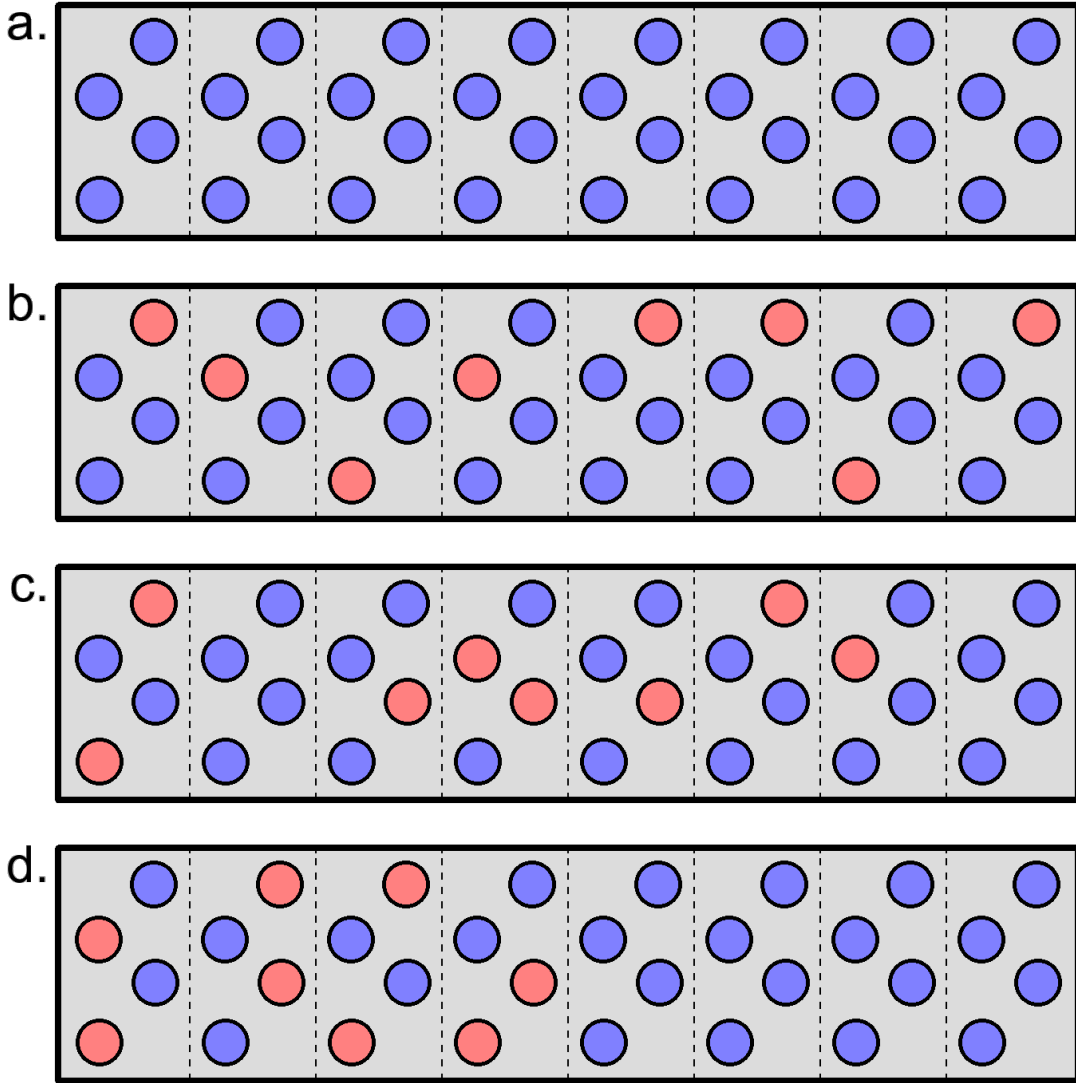


FIGURE 4.2: A cartoon showing the side view of Mg atoms in MgSiO_3 along a supercell of dimensions $8 \times 1 \times 1$, where dashed lines mark a cell boundary. **a.** shows a MgSiO_3 endmember composition (blue balls), with no Fe replacements. **b-d.** all show $(\text{Mg,Fe})\text{SiO}_3$, with 25% Fe substitution (red balls). **b.** shows a homogeneous distribution along a length unit, equal to a cell, or 1 substitution out of every possible 4 along length. **c.** shows the same Fe% concentration (8/32 replaced), but with a random distribution along the length. **d.** again has the same composition, but all the iron is clumped in the first half of the length. This scenario produces greatly differing temperature gradients on both halves when applying the direct method.

at all compositions, though the change becomes minimal at temperatures above 3000 K.

The MgSiO_3 endmember has a consistently higher conductivity than the FeSiO_3 . This can be explained by the reduction in shear modulus and increase in density associated with adding Fe, which decreases seismic velocity and thus conductivity.

The amount of Mg atoms replaced with Fe has a variable effect on conductivity.

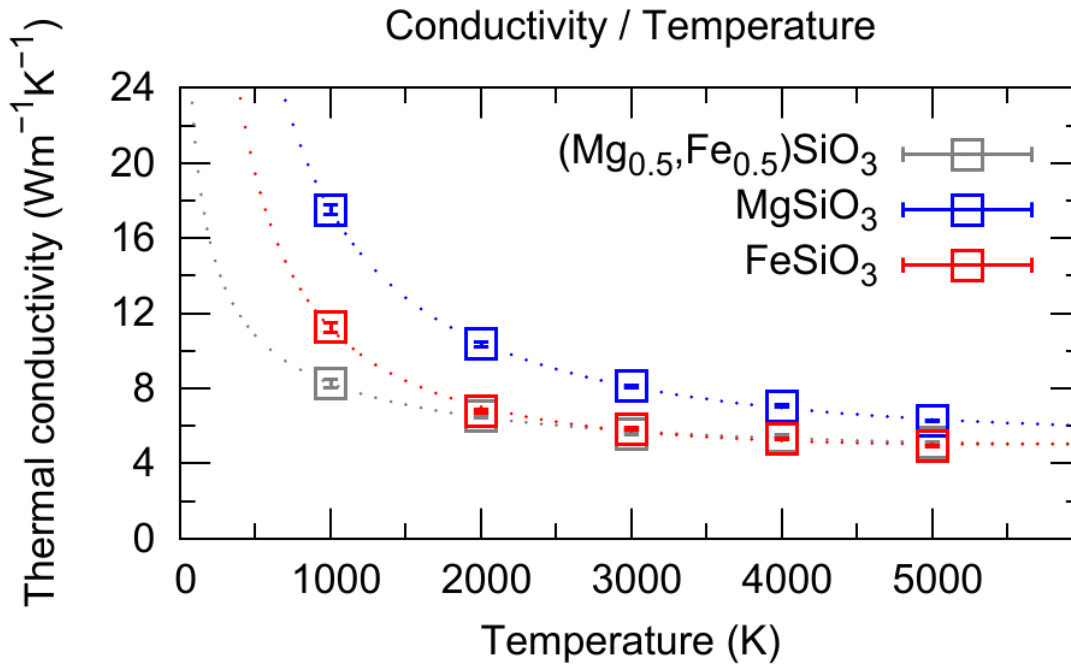


FIGURE 4.3: Data points are GK conductivity results, dotted line is the fit from Equation 4.25.

A better way to label the effect is impurities added to an endmember, i.e. Fe is added to MgSiO_3 and Mg to FeSiO_3 , which always serves increase phonon scattering and decrease conductivity. The decrease from this effect saturates towards a 50% compositional mix. At high temperatures, this effect is minimal when adding Mg to FeSiO_3 . The conductivity could already be close to its theoretical minimum due to temperature effects, little reduction is observed from adding impurities.

A simple interpolation between endmember conductivities is insufficient, the presence of a compositional mix has an effect. This effect is itself temperature-dependent, the trough-like trend flattens with increasing temperature. These temperature and compositional dependences can be combined, allowing conductivity to be determined for a range of possible CMB conditions (Figure 4.5).

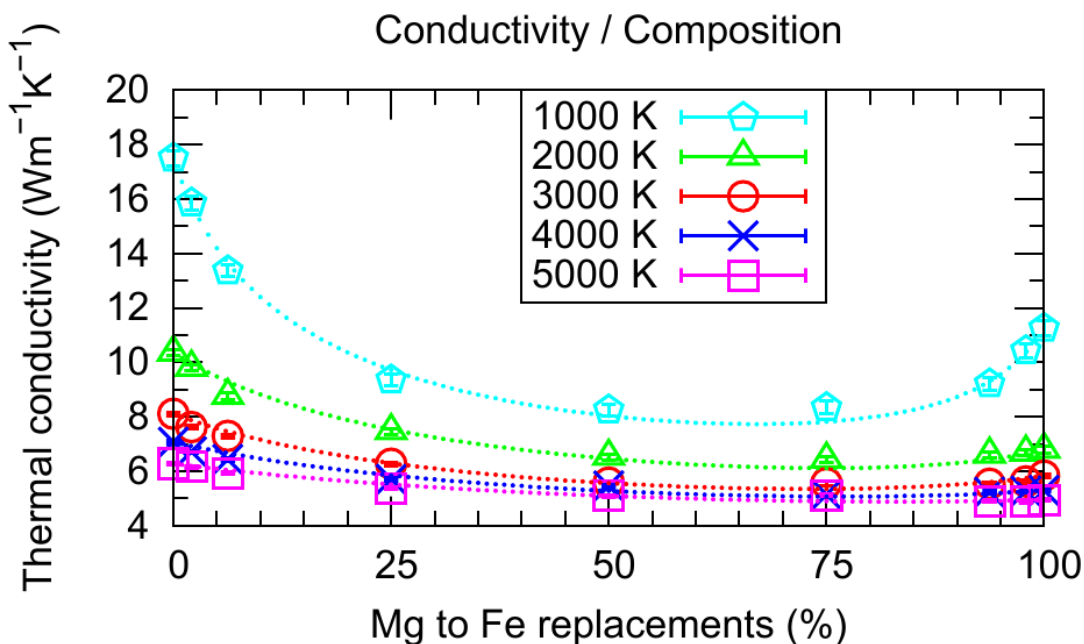


FIGURE 4.4: Computed thermal conductivities plotted as a function of Fe concentration for a range of temperatures. Dotted line for each series represents the model fit.

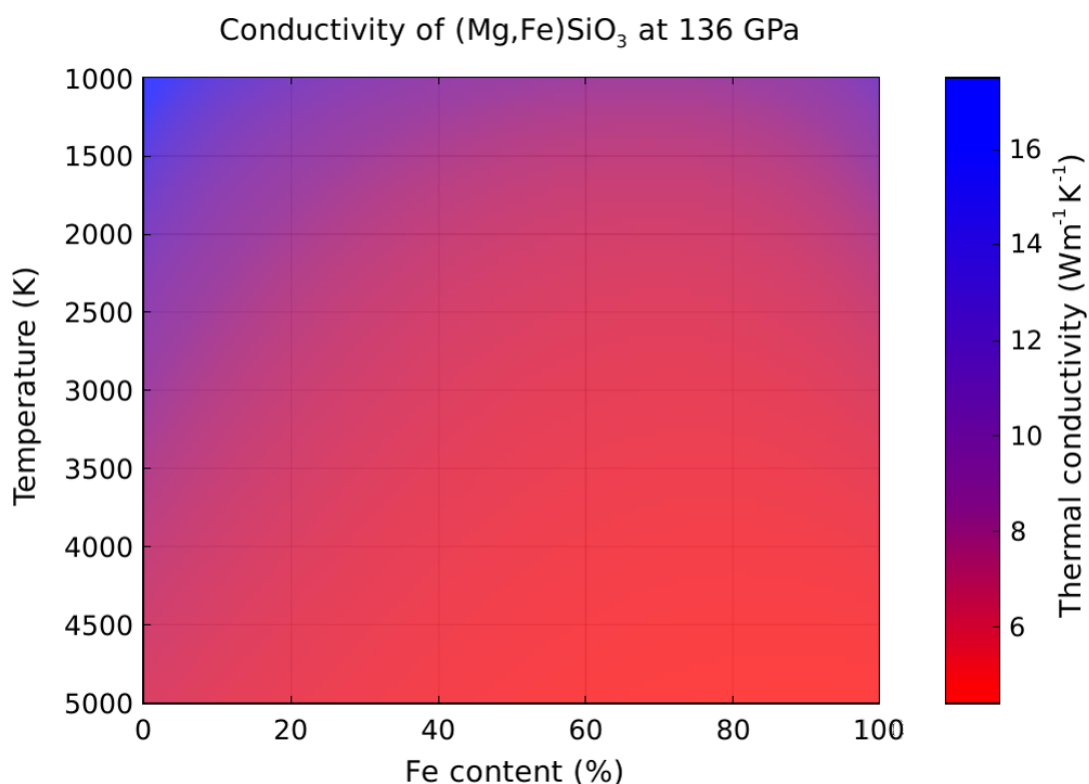


FIGURE 4.5: Modelled conductivity, shown plotted against temperature and composition. Note the sensitivity of the colour scale, showing low conductivities as dominant at high temperatures and intermediate compositions. High values are found only at low temperatures, and even then they rapidly decay and saturate to $<8\text{Wm}^{-1}\text{K}^{-1}$. Such conditions are unphysical at 136 GPa within the lower mantle.

4.4 Parameterising composition and temperature effects on CMB conductivity

In this section I develop a model for the lattice thermal conductivity of (Mg,Fe)SiO₃ perovskite at CMB conditions. Whilst the CMB is a small section of the lower mantle, it marks the heat flow boundary from core to mantle. Mantle-side thermal conductivity controls the nature of this heat flow, making it an important parameter in studies on both sides of an important interface. The CMB is isobaric at 136 GPa, and isothermal at an uncertain temperature. Fe-content can vary with position. In terms of making a model I can collect data at one pressure condition, and investigate how an array of temperatures and compositions affect thermal conductivity.

Due to uncertainty in the lower mantle's composition, properties like thermal conductivity are often averaged considering the abundance of each mineral component. There are also solid solutions to consider though, particularly the concentration of Fe in MgSiO₃, as well as the phase boundary between bridgmanite and MgSiO₃ post-perovskite.

The conductivity of an intermediate composition is not a simple weighted average of the endmember values, you cannot interpolate linearly. This can be seen in Figure 4.3, where the (Mg_{0.5},Fe_{0.5})SiO₃ results do not plot between those of MgSiO₃ and FeSiO₃.

4.4.1 Parameterising the data fit

Equations and functional forms exist for the temperature and compositional dependence of thermal conductivity, and it is possible to combine the two. The basic idea is to determine the conductivity of MgSiO₃ and FeSiO₃ endmembers at the temperature of interest, and then apply the (temperature-dependent) effect of composition.

Padture and Klemens (1997) propose a model for how impurities affect lattice thermal conductivity of a solid solution, which Ohta et al. (2017) use to fit experimental ferropericlase data. Following a similar methodology, I fit the functional form to my (Mg,Fe)SiO₃ perovskite results at various temperatures (1000 K, 2000 K, 3000 K, 4000 K, and 5000 K). In an additional step, I establish how the functional

forms change with temperature, the temperature-dependence of the compositional-dependence if you will.

Okuda et al. (2017) present a temperature scaling relation for lattice conductivity (originally from Manthilake et al., 2011), fit to their experimental results of bridgmanite. I apply this temperature scaling to computational results of MgSiO_3 and FeSiO_3 at 136 GPa. With the temperature dependence of these endmembers and of the compositional effect, I am able to determine the conductivity of any composition, interpolating to temperatures in the range 1000 K to 5000 K, at 136 GPa pressure representative of the CMB.

The aforementioned temperature dependence from Manthilake et al. (2011) considers density, allowing conductivity to be determined as a function of temperature and pressure. In the examples I will present, I am only concerned with systems at 136 GPa. All density changes will result from thermal expansion, and the equations will be altered to accomodate this.

Compositional dependence

The lattice thermal conductivity of a solid-solution as a function of temperature and composition can be approximated by the following equation (first seen as Eq. 4.2),

$$\kappa_{\text{SS}} = \kappa_{\text{V}} \left(\frac{\omega_0}{\omega_{\text{D}}} \right) \arctan \left(\frac{\omega_{\text{D}}}{\omega_0} \right), \quad (4.15)$$

where ω_0 is the phonon frequency at which the Umklapp/regular processes and impurity scattering effects' contributions to the mean free path and relaxation time (distance and time respectively travelled by a phonon) are equal. In terms of generating thermal resistance, neither effect dominates over the other at this frequency. ω_{D} is the phonon frequency corresponding to the maximum of the acoustic branch in the phonon spectrum (the Debye frequency). κ_{V} is the conductivity of the solid solution in the absence of impurity scattering (previously as Eq. 4.3, modified for the specific (Mg,Fe) SiO_3 endmembers)

$$\kappa_{\text{V}} = (1 - C) \kappa_{\text{MgSiO}_3} + C \kappa_{\text{FeSiO}_3}, \quad (4.16)$$

where C is the fractional concentration of Fe, and κ_{MgSiO_3} and κ_{FeSiO_3} the temperature dependent conductivities of the endmembers. The ratio of the phonon frequencies can be expressed as

$$\left(\frac{\omega_0}{\omega_D}\right)^2 = \frac{\chi^T}{C(1-C)}, \quad (4.17)$$

where χ is a temperature-dependent constant, and T is the temperature of interest (Padture and Klemens, 1997). χ can be thought of as a measure of resistance to the effects of impurity scattering. The κ against C relationship (Figure 4.4) shows a larger effect of impurity scattering in the form of greater curvature when T and χ are lower (see Table 4.2). For a given T and C , increasing χ causes the phonon frequency ratio $\left(\frac{\omega_0}{\omega_M}\right)$ to increase which, as discussed in Section 4.1.1, means κ_{latt} tends towards κ_i . χ is fit to the data at each temperature, but for the model we need it as a function of temperature. Figure 4.6 shows a plot of χ against T with a power law (LEFT/B.) and 4th-order polynomial (RIGHT/B.), the former of which is a poor fit and the latter an egregious overfitting.

TABLE 4.2: DOCUMENT BIT

		Temperature (K)				
		1000	2000	3000	4000	5000
Conductivity ($\text{Wm}^{-1}\text{K}^{-1}$)	Mg	17.51	10.36	8.11	7.07	6.28
	Fe	11.26	6.79	5.84	5.30	4.95
Volume (\AA^3)	Mg	5960	6017	6075	6136	6199
	Fe	6253	6310	6369	6431	6500
$V_{\text{ref}}/V(T)$	Mg	1	0.9906	0.9811	0.9714	0.9616
	Fe	1	0.9909	0.9817	0.9723	0.9619
χ		0.9973	0.9992	0.9996	0.9998	0.9999
χ^T		0.0649	0.2035	0.2748	0.4277	0.7494

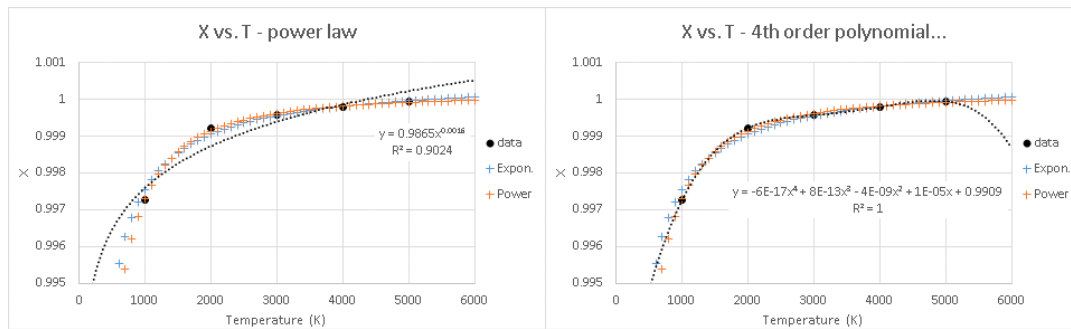


FIGURE 4.6: The fit χ values plotted against T , with power law (LEFT/A.) and 4th order polynomial (RIGHT/B.) trendlines (both black). Blue and orange series are the exponential and power law fits obtained from plotting χ^T/T (see Figure 4.7).

The lack of an obvious trend in χ against T can be mitigated by plotting χ^T over T , and fitting either a exponential or power law relationship (Figure 4.7). I use the following power law-relationship,

$$\chi^T = AT^B, \quad (4.18)$$

where A is the coefficient and B is the exponent to be determined. The magnitudes of these fit parameters are 3.468×10^{-6} and 1.426 respectively. This fit represents the temperature-dependence better, both statistically and sensitivity-wise compared to an exponential relationship ($\chi^T = Ae^{BT}$). The value of χ^T at high T has a lesser effect on the conductivity-composition relationship than at low T , where the power law fit matches the data closer. In Figure 4.6, we can see that both the power law and exponential χ^T over T relationships fit the data better than the χ over T power law or polynomial relations.

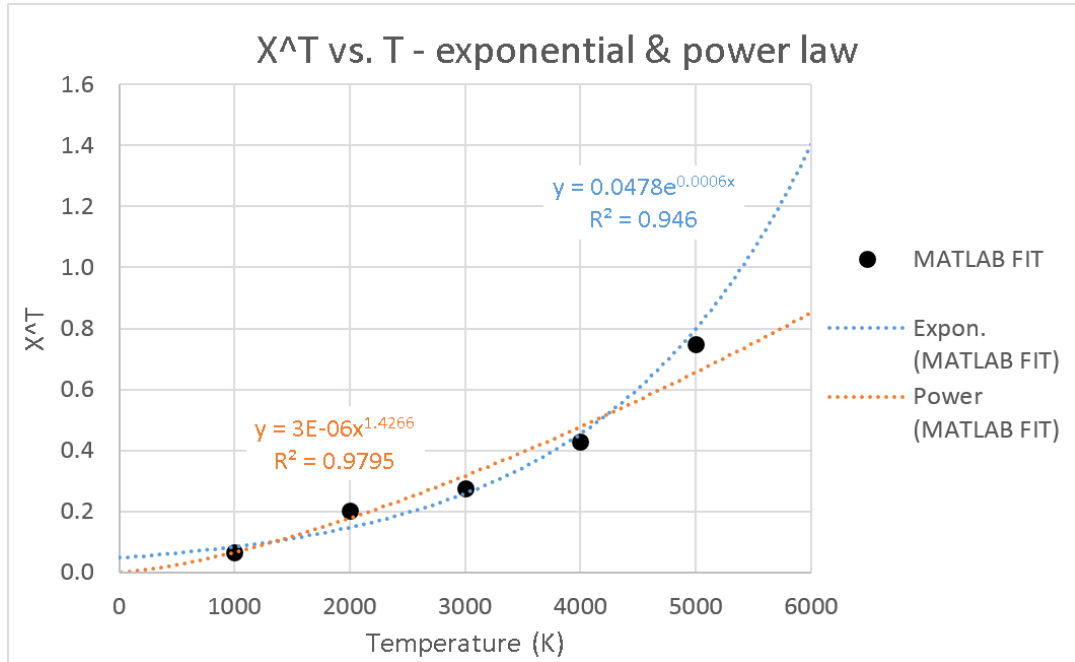


FIGURE 4.7: Exponential fit in blue (more curved), power law in orange (flatter)

Why does this model work?

At this point, we have all the pieces in place to qualitatively describe how the equation for modelling a solid solution's thermal conductivity (Eq. 4.15) works and why.

The first part is to scale a linearly interpolate the conductivity of two endmembers, at a given temperature, to the composition of interest. This (κ_V , Eq. 4.16) will be an overestimate of the true value, the conductivity is more complicated than a weighted average of the endmembers.

Increasing impurity mass difference and concentration (towards $\sim 50\%$) increase the magnitude of point defect scattering. Mass difference is always constant in this study. Concentration varies, but as discrete values across the various temperatures. For a given concentration at varying temperature, the mass difference and thus magnitude of point defect scattering is constant. Despite this, conductivity decrease due to adding impurities is not constant with varying temperature.

As temperature increases (through the range of conditions considered here) the magnitude of thermal/Umklapp scattering increases, tending to decrease conductivity (Figure. 4.3). The key thing in determining the effect of adding impurities is to consider the relative magnitudes of thermal scattering to defect scattering. As this ratio increases, with temperature, the significance of the defect scattering diminishes. An increase in thermal scattering reduces conductivity directly, but also reduces the change in conductivity associated with adding impurities.

This can be seen in Figure. 4.4, where the actual conductivity and curvature of the model fit decrease with temperature. “Curvature” in this sense can be measured by the area between the model and a straight line between endmembers. The model becomes more similar to the endmember line (area decrease) as temperature increases, as the effect of thermal scattering increases relative to defect scattering. An additional diagram is provided in Figure 4.8, showing how the

In the context of the model, the effect of this ratio is handled by the arctan segment of Eq. 4.15 (as alluded to in Figure. 4.2). The (ω_0/ω_D) term (Eq. 4.17) contains the temperature and chemical (χ), and concentration (C) variables to control the scaling effect on κ_V .

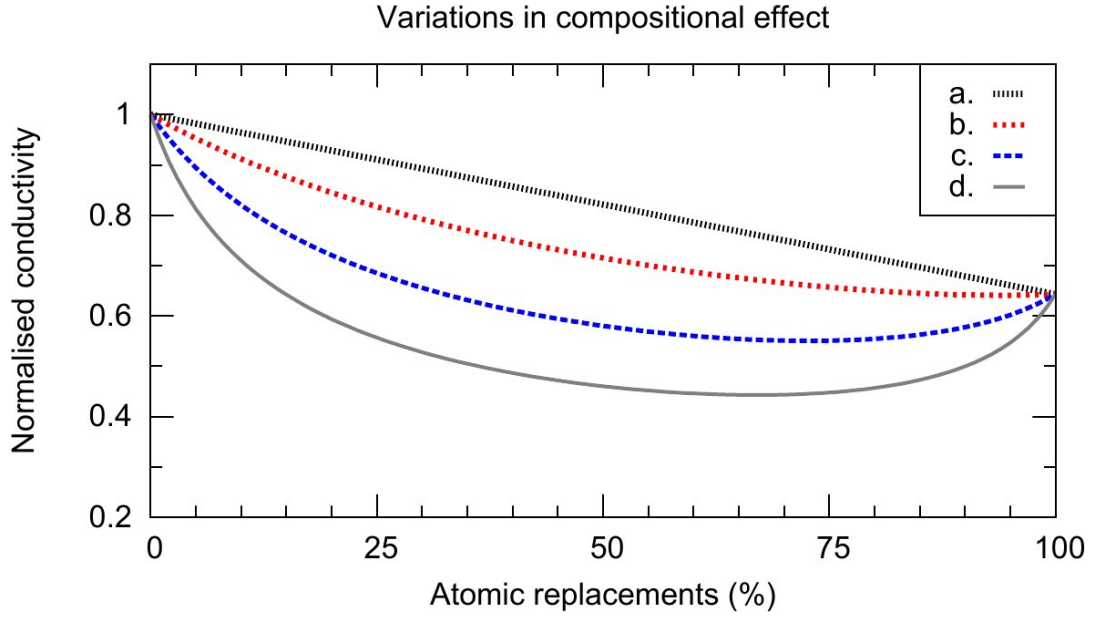


FIGURE 4.8: A graph showing how the relative magnitudes of defect and thermal scattering affect the resultant conductivity. Conductivity values are normalised to the maximum, the MgSiO_3 value in this case. This figure does not show how the magnitude of conductivity variations with temperature, but the magnitude of conductivity changes from adding impurities.

a. shows the compositionally-weighted average of endmember conductivities. It represents the conductivity in absence of defect scattering, but with the addition of heavier Fe atoms having the effect of reducing conductivity.

d. represents conductivity if impurity scattering were to dominate over Umklapp processes. As with **a.**, this series is hypothetical, and the physical result lies somewhere inbetween the two.

b. & **c.** represent a solid solution at hot and cold conditions respectively. **b.** would be found at a higher temperature, where increased thermal scattering reduces the significance of defect scattering. **c.** represents a colder condition with fewer Umklapp processes, where impurities are more relevant and there is a larger decrease relative to **a.**, compared to the hot case (**b.**).

Temperature dependence

The conductivities of κ_{MgSiO_3} and κ_{FeSiO_3} from Equation 4.16 can be scaled with temperature, giving an adjusted value

$$\kappa_{\text{adj}} = \kappa_{\text{ref}} \left(\frac{\rho}{\rho_{\text{ref}}} \right)^g \left(\frac{T_{\text{ref}}}{T} \right)^a. \quad (4.19)$$

ρ is density, g and a are exponents which control the nature of the density and temperature-dependence, and “ref” denotes a reference value (Manthilake et al., 2011; Okuda et al., 2017). This equation is fit to the data, anchored around the values

of the reference data point (the fit is shown in Figure 4.3). I fit to the data point at 1000 K, as the conductivities at higher temperatures become more similar, converging towards a minimum point. Anchoring to 1000 K reduces the error in the fit, on account of the relatively larger conductivity at this temperature.

For a given composition, the mass of the simulated system does not change with temperature. The number and type of atoms remains constant, while thermal effects cause density variations. The density relation in Equation 4.19 can be reformulated as

$$\frac{\rho}{\rho_{\text{ref}}} \equiv \frac{V_{\text{ref}}}{V}, \quad (4.20)$$

because $\rho \propto V^{-1}$, where V is the volume of the system in question. This leads to a modified version of Equation 4.19

$$\kappa_{\text{adj}} = \kappa_{\text{ref}} \left(\frac{V_{\text{ref}}}{V} \right)^g \left(\frac{T_{\text{ref}}}{T} \right)^a. \quad (4.21)$$

The exponent g (Manthilake et al., 2011) represents the rate of change of lattice thermal conductivity with density, at a constant temperature,

$$g = (\partial \ln \kappa_{\text{latt}} / \partial \ln \rho)_T. \quad (4.22)$$

The density/volume changes that I observe result from thermal effects, i.e. not at a constant temperature and not pressure-driven. The rate of change in conductivity with density in my data are better represented as something like

$$h \sim (\partial \ln \kappa_{\text{latt}} / \partial \ln \rho)_P, \quad (4.23)$$

where pressure (P) is the condition kept constant. The significance here is that pressure-driven and temperature-driven density changes affect the conductivity differently. At constant temperature, conductivity and density increase with pressure. The opposite is true at constant pressure for the material and temperatures considered here, conductivity and density decrease with increasing temperature. The result is g and h having opposite polarities based on the scenarios they describe.

Volume does not need to be input ((INDEPENDENT?)) variable for the model,

as all the data are obtained from constant pressure (136 GPa) calculations and any volume variations relate to thermal expansion. I express the volume ratio shown in Equation 4.21 as

$$\frac{V_{\text{ref}}}{V(T)} \approx mT + c, \quad (4.24)$$

a simple linear function of temperature (see Figure 4.9), where m is the gradient and c the intercept (as you might expect).

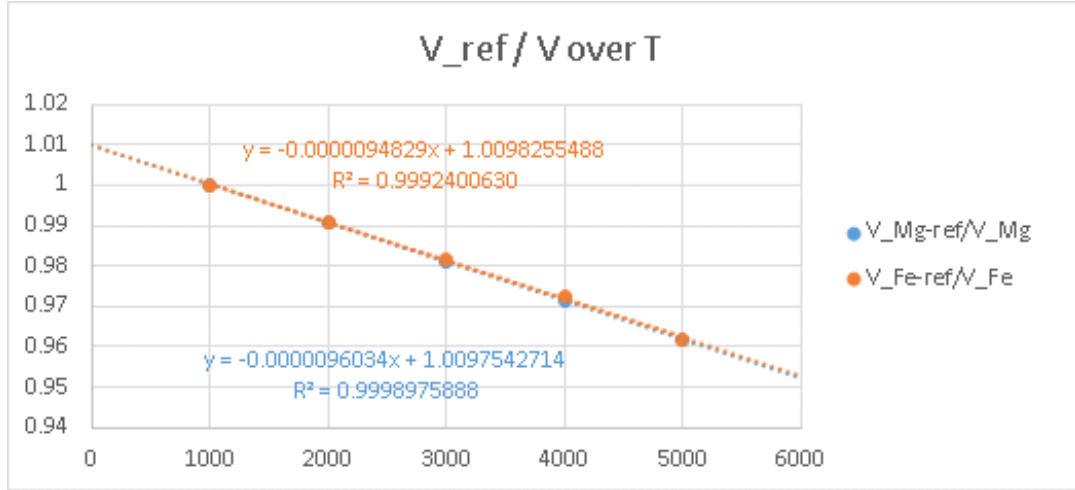


FIGURE 4.9: V_{ref}/V can be expressed as a simple linear function of T .

With Equation 4.24, we rewrite Equation 4.19 one more time,

$$\kappa_{\text{adj}} = \kappa_{\text{ref}} (mT + c)^h \left(\frac{T_{\text{ref}}}{T} \right)^a. \quad (4.25)$$

This equation allows me to obtain a conductivity value at any temperature within the fit range, comprising a reference conductivity and temperature for the material in question, with constants (m , c , h , & a , see Table 4.3) fit to data across a range of temperatures. This scaling process is necessary to obtain κ_{MgSiO_3} and κ_{FeSiO_3} , which have their own reference values and fit constants, for use in Eq. 4.16.

4.4.2 MEAN FREE PATH

MFP FROM DM EXTRAPOLATION

REFERENCE SCHELLING FOR EQUATION

TABLE 4.3: Mg and Fe refer to MgSiO₃ and FeSiO₃ endmembers, SS the solid solution with a 50% mix.

	Composition		
	Mg	SS	Fe
κ_{ref}	17.51	8.26	11.26
h	-10.93	-5.52	-17.32
a	0.896	0.428	0.913
m	-9.60E-06	-9.47E-06	-9.48E-06
c	1.00975	1.00965	1.00983

The conductivities from supercells (κ_L) of varying length (L) obtained via direct method calculations fit the form (modified from Stackhouse and Stixrude, 2010)

$$\frac{1}{\kappa_L} = \left[\frac{12}{C_v v} \right] \frac{1}{L} + \left[\frac{3}{C_v v} \frac{1}{\Lambda_{ph-ph}} \right], \quad (4.26)$$

where C_v is the volumetric isochoric heat capacity, v is the phonon group velocity, and Λ_{ph-ph} is the mean free path associated with phonon–phonon scattering. When the inverse conductivities are plotted against the inverse cell lengths, extrapolation to the y-axis ($1/L = 0$) gives the bulk material ($L \rightarrow \infty$) conductivity, and its associated phonon mean free path. The two square-bracketed terms in the above equation represent the gradient and intercept respectively, of such a line fit to data and extrapolated ((FIGURE)).

I can rewrite Equation 4.26 with the following simplifications

$$M = \left[\frac{12}{C_v v} \right], \text{ and } \frac{M}{4} = \frac{3}{C_v v},$$

giving

$$\frac{1}{\kappa_L} = M \frac{1}{L} + \left[\frac{M}{4} \frac{1}{\Lambda_{ph-ph}} \right].$$

When $1/L = 0$, the extrapolated conductivity can be equated to the gradient and effective mean free path

$$\frac{1}{\kappa} = \frac{M}{4} \frac{1}{\Lambda},$$

and thus

$$\Lambda = \frac{M}{4} \kappa.$$

Using the gradient and conductivity from direct method calculations at 136 GPa,

4000 K, and a supercell cross-sectional area of 12×12 , the mean free path is equal to 0.23 ± 0.03 nm. This value is roughly half the width of the unit cell in the A/x-direction, or the width of a direct method temperature section.

SCALING MFP TO QUANTIFY PHONON-DEFECT SCATTERING

This MFP value is obtained from a conductivity representative of bulk MgSiO_3 bridgmanite, therefore I can assume it is the effective MFP in the absense of phonon-defect or phonon-boundary scattering ((MATTHIESEN)). MFP is direct proportional to conductivity ((REF)), therefore I propose scaling the 4000 K GK conductivity results ((REF)) to try and quantify the phonon-defect scattering associated with adding iron. When considering the effect of impurities on conductivity, the effective MFP depends on phonon-phonon and phonon-defect interactions

$$\frac{1}{\Lambda} = \frac{1}{\Lambda_{\text{ph-ph}}} + \frac{1}{\Lambda_{\text{ph-d}}} .$$

The MFP determined from the direct method extrapolation can be matched with the equivalent 0% Fe, 4000 K Green-Kubo result on Figure REF. If $7.07 \text{ Wm}^{-1}\text{K}^{-1}$ is proportional to an effective MFP of 0.23 nm, I can scale this MFP value by the MgSiO_3 endmember-normalised conductivities ((ADD FIGURE)).

I make the assumption that the data points/curve of Figure REF represent the effective MFP, the linear interpolation between endmembers the phonon-phonon scattering MFP. The interpolated conductivities do not capture the non-linear effects of defect scattering, at constant temperature the change in conductivity is proportional to the change in mass associated with changing Mg to Fe.

The deficit between computed and interpolated conductivity can be imagined as phonon-defect contribution to Λ , the bigger the gap at a given composition, the greater significance of $\Lambda_{\text{ph-d}}$. I will obtain the phonon-defect MFP by subtracting the inverse of the two, as in

$$\frac{1}{\Lambda_{\text{ph-d}}} = \frac{1}{\Lambda} - \frac{1}{\Lambda_{\text{ph-ph}}} .$$

C(1-C) MODEL LIMITATIONS

Using this method to determine $\Lambda_{\text{ph-d}}$, I am able to observe how its magnitude changes with composition. Taking the 4000 K model-fit conductivities, the largest effect of phonon-defect scattering (smallest MFP) is at a composition around 50%. This is to be expected, and is set by the $C(1 - C)$ term in Equation REF. However, when the raw 4000 K data is used to determine $\Lambda_{\text{ph-d}}$, the greatest effect is at a composition between 25% and 50% (albeit closer to 25%). The model is assuming that an equal number of each type of atom creates the most phonon-defect scattering, but I believe it is when each type of atom contributes equal to the system's mass ((INFORMAL, THERE IS SCIENCE TO BACK THIS UP SOMEWHERE)). The composition at which this mass contribution scenario is satisfied can be calculated by

$$C_{\text{mass}} = \frac{A_{\text{Mg}}}{A_{\text{Mg}} + A_{\text{Fe}}} ,$$

where A is atomic mass, Mg corresponds to $C = 0$ and Fe to $C = 1$. For Mg and Fe, $C_{\text{mass}} = 0.3$, or 30% Fe to 70% Mg. This is the turning point in phonon-defect scattering, it increases up to this composition, and decreases after. Even if conductivity decreases overall due to phonon-phonon effects, this is the point of minimum $\Lambda_{\text{ph-d}}$.

DM ANALYSIS - PH-B SCATTERING AND SHORTEST CELL

WORK OUT A TON OF DM MFPs???

I can do something similar with direct method results, taking the extrapolated MFP as the phonon-phonon contribution (as in Equation 4.26), and the computed conductivity as the effective. Subtracting these two may give info on the effects of phonon-boundary scattering, for impurity-free systems anyway.

MASS VS. POTENTIAL IN MODELLING FE

I believe mass is the most important thing for the magnitude of phonon-defect scattering. I am to prove this by running calculations where the mass of the impurities are kept the same as Mg, only changing their potential to match my fitted Mg-Fe

interaction. I predict conductivity will be largely unchanged with varying composition.

Chapter 5

Modelling the lower mantle with variable thermal conductivity

5.1 Main Section 1

Lorem ipsum dolor sit amet, consectetur adipiscing elit. Aliquam ultricies lacinia euismod. Nam tempus risus in dolor rhoncus in interdum enim tincidunt. Donec vel nunc neque. In condimentum ullamcorper quam non consequat. Fusce sagittis tempor feugiat. Fusce magna erat, molestie eu convallis ut, tempus sed arcu. Quisque molestie, ante a tincidunt ullamcorper, sapien enim dignissim lacus, in semper nibh erat lobortis purus. Integer dapibus ligula ac risus convallis pellentesque.

5.1.1 Subsection 1

Nunc posuere quam at lectus tristique eu ultrices augue venenatis. Vestibulum ante ipsum primis in faucibus orci luctus et ultrices posuere cubilia Curae; Aliquam erat volutpat. Vivamus sodales tortor eget quam adipiscing in vulputate ante ullamcorper. Sed eros ante, lacinia et sollicitudin et, aliquam sit amet augue. In hac habitasse platea dictumst.

Chapter 6

Summary/Discussion/Conclusion

6.1 Main Section 1

Lorem ipsum dolor sit amet, consectetur adipiscing elit. Aliquam ultricies lacinia euismod. Nam tempus risus in dolor rhoncus in interdum enim tincidunt. Donec vel nunc neque. In condimentum ullamcorper quam non consequat. Fusce sagittis tempor feugiat. Fusce magna erat, molestie eu convallis ut, tempus sed arcu. Quisque molestie, ante a tincidunt ullamcorper, sapien enim dignissim lacus, in semper nibh erat lobortis purus. Integer dapibus ligula ac risus convallis pellentesque.

6.1.1 Subsection 1

Nunc posuere quam at lectus tristique eu ultrices augue venenatis. Vestibulum ante ipsum primis in faucibus orci luctus et ultrices posuere cubilia Curae; Aliquam erat volutpat. Vivamus sodales tortor eget quam adipiscing in vulputate ante ullamcorper. Sed eros ante, lacinia et sollicitudin et, aliquam sit amet augue. In hac habitasse platea dictumst.

Appendix A

Frequently Asked Questions

A.1 How do I change the colors of links?

The color of links can be changed to your liking using:

```
\hypersetup{urlcolor=red}, or  
\hypersetup{citecolor=green}, or  
\hypersetup{allcolor=blue}.
```

If you want to completely hide the links, you can use:

```
\hypersetup{allcolors=.}, or even better:  
\hypersetup{hidelinks}.
```

If you want to have obvious links in the PDF but not the printed text, use:

```
\hypersetup{colorlinks=false}.
```


Bibliography

- Ammann, M. W. et al. (2014). "Variation of thermal conductivity and heat flux at the Earth's core mantle boundary". In: *Earth and Planetary Science Letters* 390, pp. 175–185. ISSN: 0012821X. DOI: [10.1016/j.epsl.2014.01.009](https://doi.org/10.1016/j.epsl.2014.01.009). URL: <http://linkinghub.elsevier.com/retrieve/pii/S0012821X14000120>.
- Balandin, A. A. et al. (2008). "Superior thermal conductivity of single-layer graphene." In: *Nano letters* 8.3, pp. 902–907. ISSN: 1530-6984. DOI: [10.1021/nl10731872](https://doi.org/10.1021/nl10731872). URL: <http://www.ncbi.nlm.nih.gov/pubmed/18284217>.
- Brodholt, J. P. (2000). "Pressure-induced changes in the compression mechanism of aluminous perovskite in the Earth's mantle". In: *Nature* 407.6804, pp. 620–622. ISSN: 00280836. DOI: [10.1038/35036565](https://doi.org/10.1038/35036565).
- Brown, J. M. and R. G. McQueen (1986). "Phase transitions, Grüneisen parameter, and elasticity for shocked iron between 77~GPa and 400~GPa". In: *Journal of Geophysical Research* 91.B7, pp. 7485–7494.
- Dalton, D. A. et al. (2013). "Effect of mass disorder on the lattice thermal conductivity of MgO periclase under pressure." In: *Scientific reports* 3, pp. 2400–2405. ISSN: 2045-2322. DOI: [10.1038/srep02400](https://doi.org/10.1038/srep02400). URL: <http://www.pubmedcentral.nih.gov/articlerender.fcgi?artid=3739002&tool=pmcentrez&rendertype=abstract>.
- Dekura, H., T. Tsuchiya, and J. Tsuchiya (2013). "Ab initio lattice thermal conductivity of MgSiO₃ perovskite as found in Earth's lower mantle". In: *Physical Review Letters* 110, pp. 1–5. ISSN: 0031-9007. DOI: [10.1103/PhysRevLett.110.025904](https://doi.org/10.1103/PhysRevLett.110.025904). URL: <http://link.aps.org/doi/10.1103/PhysRevLett.110.025904>.
- Dobson, D. P. and J. P. Brodholt (2005). "Subducted banded iron formations as a source of ultralow-velocity zones at the core-mantle boundary". In: *Nature* 434, pp. 371–374. DOI: [10.1038/nature03385](https://doi.org/10.1038/nature03385).

- Dubuffet, F. and D. A. Yuen (2000). "A thick pipe-like heat-transfer mechanism in the mantle: Nonlinear coupling between 3-D convection and variable thermal conductivity". In: *Geophysical research letters* 27, pp. 17–20. URL: <http://onlinelibrary.wiley.com/doi/10.1029/1999GL008338/full>.
- Gale, J. D. (1997). "GULP: A computer program for the symmetry-adapted simulation of solids". In: *J. Chem. Soc.* 93, pp. 629–637.
- Garnero, E. J. and A. K. McNamara (2008). "Structure and dynamics of Earth's lower mantle". In: *Science* 320, pp. 626–629. URL: <http://www.sciencemag.org/content/320/5876/626.short>.
- Goncharov, A. F. et al. (2008). "Radiative conductivity in the Earth's lower mantle." In: *Nature* 456, pp. 231–234. ISSN: 1476-4687. DOI: [10.1038/nature07412](https://doi.org/10.1038/nature07412). URL: <http://www.ncbi.nlm.nih.gov/pubmed/19005553>.
- Goncharov, A. F. et al. (2009). "Thermal conductivity of lower-mantle minerals". In: *Physics of the Earth and Planetary Interiors* 174, pp. 24–32. ISSN: 00319201. DOI: [10.1016/j.pepi.2008.07.033](https://doi.org/10.1016/j.pepi.2008.07.033). URL: <http://linkinghub.elsevier.com/retrieve/pii/S0031920108001945>.
- Green, M. S. (1954). "Markoff random processes and the statistical mechanics of time-dependent phenomena. II. Irreversible processes in fluids". In: *The Journal of Chemical Physics* 22.3, pp. 398–413. ISSN: 00219606. DOI: [10.1063/1.1740082](https://doi.org/10.1063/1.1740082).
- Gubbins, D., A. P. Willis, and B. Sreenivasan (2007). "Correlation of Earth's magnetic field with lower mantle thermal and seismic structure". In: *Physics of the Earth and Planetary Interiors* 162, pp. 256–260. ISSN: 00319201. DOI: [10.1016/j.pepi.2007.04.014](https://doi.org/10.1016/j.pepi.2007.04.014). URL: <http://linkinghub.elsevier.com/retrieve/pii/S0031920107000908>.
- Haigis, V. (2013). "Trace elements in silicate melts and the thermal conductivity of the earth's deep mantle: insights from atomistic modeling of geomaterials". PhD thesis. Freien Universität Berlin, p. 83. URL: <http://d-nb.info/1031915087/>.
- Haigis, V., M. Salanne, and S. Jahn (2012). "Thermal conductivity of MgO, MgSiO₃ perovskite and post-perovskite in the Earth's deep mantle". In: *Earth and Planetary Science Letters* 355–356, pp. 102–108. ISSN: 0012821X. DOI: [10.1016/j.epsl.2012.09.002](https://doi.org/10.1016/j.epsl.2012.09.002). URL: <http://linkinghub.elsevier.com/retrieve/pii/S0012821X12004815>.

- Hofmeister, A. M. (1999). "Mantle values of thermal conductivity and the geotherm from phonon lifetimes". In: *Science* 283, pp. 1699–1706. ISSN: 00368075. DOI: [10.1126/science.283.5408.1699](https://doi.org/10.1126/science.283.5408.1699). URL: <http://www.sciencemag.org/cgi/doi/10.1126/science.283.5408.1699>.
- Howell, P. C. (2012). "Comparison of molecular dynamics methods and interatomic potentials for calculating the thermal conductivity of silicon." In: *The Journal of chemical physics* 137.22, p. 224111. ISSN: 1089-7690. DOI: [10.1063/1.4767516](https://doi.org/10.1063/1.4767516). URL: <http://www.ncbi.nlm.nih.gov/pubmed/23248991>.
- Hu, L., W. J. Evans, and P. Keblinski (2011). "One-dimensional phonon effects in direct molecular dynamics method for thermal conductivity determination". In: *Journal of Applied Physics* 110.11, p. 113511. ISSN: 00218979. DOI: [10.1063/1.3660234](https://doi.org/10.1063/1.3660234). URL: <http://scitation.aip.org/content/aip/journal/jap/110/11/10.1063/1.3660234>.
- Keppler, H. et al. (2008). "Optical absorption and radiative thermal conductivity of silicate perovskite to 125 gigapascals". In: *Science* 322, pp. 1529–1532. URL: <http://www.sciencemag.org/content/322/5907/1529.short>.
- Klemens, P. G. (1960). "Thermal resistance due to point defects at high temperatures". In: *Physical Review* 119.2, pp. 507–509. ISSN: 0031-899X. DOI: [10.1103/PhysRev.119.507](https://doi.org/10.1103/PhysRev.119.507). URL: <http://link.aps.org/doi/10.1103/PhysRev.119.507>.
- Koker, N. de (2009). "Thermal conductivity of MgO periclase from equilibrium first principles molecular dynamics". In: *Physical Review Letters* 103.12, pp. 1–4. DOI: [10.1103/PhysRevLett.103.125902](https://doi.org/10.1103/PhysRevLett.103.125902).
- Kubo, R. (1957). "Statistical-mechanical theory of irreversible processes. I." In: *Journal of the Physical Society of Japan* 12.6, pp. 570–586. DOI: [10.1143/JPSJ.12.570](https://doi.org/10.1143/JPSJ.12.570).
- (1966). "The fluctuation-dissipation theorem". In: *Rep. Prog. Phys.* 29.1, p. 255. ISSN: 00319007.
- Lay, T. et al. (2006). "A post-perovskite lens and D" heat flux beneath the central Pacific." In: *Science* 314, pp. 1272–1276. ISSN: 1095-9203. DOI: [10.1126/science.1133280](https://doi.org/10.1126/science.1133280). URL: <http://www.ncbi.nlm.nih.gov/pubmed/17124317>.
- Lay, T., J. Hernlund, and B. A. Buffett (2008). "Core–mantle boundary heat flow". In: *Nature Geoscience* 1, pp. 25–32. ISSN: 1752-0894. DOI: [10.1038/ngeo.2007.44](https://doi.org/10.1038/ngeo.2007.44). URL: <http://www.nature.com/doifinder/10.1038/ngeo.2007.44>.

- Lee, D. et al. (1995). "Thermal characterization of carbon-opacified silica aerogels". In: *Journal of Non-Crystalline Solids* 186, pp. 285–290. ISSN: 00223093. DOI: [10.1016/0022-3093\(95\)00055-0](https://doi.org/10.1016/0022-3093(95)00055-0). URL: <http://linkinghub.elsevier.com/retrieve/pii/0022309395000550>.
- Manthilake, G. M. et al. (2011). "Lattice thermal conductivity of lower mantle minerals and heat flux from Earth's core." In: *Proceedings of the National Academy of Sciences of the United States of America* 108, pp. 1–4. ISSN: 1091-6490. DOI: [10.1073/pnas.1110594108](https://doi.org/10.1073/pnas.1110594108). URL: <http://www.pubmedcentral.nih.gov/articlerender.fcgi?artid=3207700&tool=pmcentrez&rendertype=abstract>.
- Mao, W. L. et al. (2004). "Ferromagnesian post-perovskite silicates in the D" layer of the Earth". In: *Proceedings of the National Academy of Sciences* 101.45, pp. 15867–15869. ISSN: 0027-8424. DOI: [10.1073/pnas.0407135101](https://doi.org/10.1073/pnas.0407135101). URL: <http://www.pnas.org/cgi/doi/10.1073/pnas.0407135101>.
- Müller-Plathe, F. (1997). "A simple nonequilibrium molecular dynamics method for calculating the thermal conductivity". In: *The Journal of Chemical Physics* 106.14, p. 6082. ISSN: 00219606. DOI: [10.1063/1.473271](https://doi.org/10.1063/1.473271). URL: <http://scitation.aip.org/content/aip/journal/jcp/106/14/10.1063/1.473271>.
- Murakami, M. et al. (2004). "Post-perovskite phase transition in MgSiO₃". In: *Science* 304, pp. 855–858.
- Naliboff, J. B. and L. H. Kellogg (2006). "Dynamic effects of a step-wise increase in thermal conductivity and viscosity in the lowermost mantle". In: *Geophysical Research Letters* 33, pp. 1–4. ISSN: 0094-8276. DOI: [10.1029/2006GL025717](https://doi.org/10.1029/2006GL025717). URL: <http://doi.wiley.com/10.1029/2006GL025717>.
- Nieto-Draghi, C. and J. B. Avalos (2013). "Non-equilibrium momentum exchange algorithm for molecular dynamics simulation of heat flow in multicomponent systems". In: *Molecular Physics* 101.14, pp. 2303–2307. DOI: [10.1080/0026897031000154338](https://doi.org/10.1080/0026897031000154338).
- Oganov, A. R. and S. Ono (2004). "Theoretical and experimental evidence for a post-perovskite phase of MgSiO₃ in Earth's D" layer". In: *Nature* 430, pp. 445–448.
- Oganov, A. R., J. P. Brodholt, and D. G. Price (2000). "Comparative study of quasiharmonic lattice dynamics, molecular dynamics and Debye model applied to MgSiO₃ perovskite". In: *Physics of the Earth and Planetary Interiors* 122, pp. 277–288. URL: <http://www.sciencedirect.com/science/article/pii/S0031920100001977>.

- Ohta, K. et al. (2012). "Lattice thermal conductivity of MgSiO₃ perovskite and post-perovskite at the core–mantle boundary". In: *Earth and Planetary Science Letters* 349-350, pp. 109–115. ISSN: 0012821X. DOI: [10.1016/j.epsl.2012.06.043](https://doi.org/10.1016/j.epsl.2012.06.043). URL: <http://linkinghub.elsevier.com/retrieve/pii/S0012821X12003354>.
- Ohta, K., T. Yagi, and K. Hirose (2014). "Thermal diffusivities of MgSiO₃ and Al-bearing MgSiO₃ perovskites". In: *American Mineralogist* 99, pp. 94–97. URL: <http://www.degruyter.com/view/j/am.2014.99.issue-1/ammin.2014.4598/ammin.2014.4598.xml>.
- Ohta, K. et al. (2017). "Thermal conductivity of ferropericlase in the Earth's lower mantle". In: *Earth and Planetary Science Letters* 465, pp. 29–37. ISSN: 0012821X. DOI: [10.1016/j.epsl.2017.02.030](https://doi.org/10.1016/j.epsl.2017.02.030). URL: <http://dx.doi.org/10.1016/j.epsl.2017.02.030>.
- Okuda, Y. et al. (2017). "The effect of iron and aluminum incorporation on lattice thermal conductivity of bridgmanite at the Earth's lower mantle". In: *Earth and Planetary Science Letters* 474, September, pp. 25–31. ISSN: 0012821X. DOI: [10.1016/j.epsl.2017.06.022](https://doi.org/10.1016/j.epsl.2017.06.022). URL: <http://dx.doi.org/10.1016/j.epsl.2017.06.022>.
- Osako, M. and E. Ito (1991). "Thermal diffusivity of MgSiO₃ perovskite". In: *Geophysical Research Letters* 18, pp. 239–242. URL: <http://onlinelibrary.wiley.com/doi/10.1029/91GL00212/full>.
- Padture, N. P. and P. G. Klemens (1997). "Low thermal conductivity in garnets". In: *Journal of the American Ceramic Society* 80.4, pp. 1018–1020. ISSN: 00027820. DOI: [10.1111/j.1151-2916.1997.tb02937.x](https://doi.org/10.1111/j.1151-2916.1997.tb02937.x).
- Parise, J. B. and Y. Wang (1990). "Crystal structure and thermal expansion of (Mg,Fe)SiO₃ perovskite". In: *October* 12, pp. 2089–2092.
- Plimpton, S. (1995). "Fast parallel algorithms for short-range molecular dynamics". In: *Journal of Computational Physics* 117, pp. 1–19. ISSN: 00219991. DOI: [10.1006/jcph.1995.1039](https://doi.org/10.1006/jcph.1995.1039).
- Schelling, P. K., S. R. Phillpot, and P. Keblinski (2002). "Comparison of atomic-level simulation methods for computing thermal conductivity". In: *Physical Review B* 65.14, p. 144306. ISSN: 1098-0121. DOI: [10.1103/PhysRevB.65.144306](https://doi.org/10.1103/PhysRevB.65.144306). URL: <http://link.aps.org/doi/10.1103/PhysRevB.65.144306>.

- Sellan, D. P. et al. (2010). "Size effects in molecular dynamics thermal conductivity predictions". In: *Physical Review B* 81, pp. 1–10. ISSN: 1098-0121. DOI: [10.1103/PhysRevB.81.214305](https://doi.org/10.1103/PhysRevB.81.214305). URL: <http://link.aps.org/doi/10.1103/PhysRevB.81.214305>.
- Snyder, G. J. and E. S. Toberer (2008). "Complex thermoelectric materials". In: *Nature materials* 7.2, pp. 105–114. ISSN: 1476-1122. DOI: [10.1038/nmat2090](https://doi.org/10.1038/nmat2090). arXiv: [1512.00567](https://arxiv.org/abs/1512.00567).
- Stackhouse, S. and L. Stixrude (2010). "Theoretical methods for calculating the lattice thermal conductivity of minerals". In: *Reviews in Mineralogy and Geochemistry* 71, pp. 253–269. ISSN: 1529-6466. DOI: [10.2138/rmg.2010.71.12](https://doi.org/10.2138/rmg.2010.71.12). URL: <http://rimg.geoscienceworld.org/cgi/doi/10.2138/rmg.2010.71.12>.
- Stackhouse, S., L. Stixrude, and B. B. Karki (2015). "First-principles calculations of the lattice thermal conductivity of the lower mantle". In: *Earth And Planetary Science Letters* 427, pp. 11–17. ISSN: 0012821X. DOI: [10.1016/j.epsl.2015.06.050](https://doi.org/10.1016/j.epsl.2015.06.050). URL: <http://dx.doi.org/10.1016/j.epsl.2015.06.050>.
- Tang, X. and J. Dong (2009). "Pressure dependence of harmonic and anharmonic lattice dynamics in MgO: A first-principles calculation and implications for lattice thermal conductivity". In: *Physics of the Earth and Planetary Interiors* 174, pp. 33–38. ISSN: 00319201. DOI: [10.1016/j.pepi.2008.10.003](https://doi.org/10.1016/j.pepi.2008.10.003).
- (2010). "Lattice thermal conductivity of MgO at conditions of Earth's interior". In: *Proceedings of the National Academy of Sciences* 107.10, pp. 4539–4543. ISSN: 0027-8424. DOI: [10.1073/pnas.0907194107](https://doi.org/10.1073/pnas.0907194107). URL: <http://www.pnas.org/cgi/doi/10.1073/pnas.0907194107>.
- Tang, X. et al. (2014). "The thermal conductivity of the Earth's lower mantle". In: *Geophysical Research Letters* 41, pp. 2746–2752. DOI: [10.1002/2014GL059385](https://doi.org/10.1002/2014GL059385). Received. URL: <http://onlinelibrary.wiley.com/doi/10.1002/2014GL059385/pdf>.
- Thomas, J. A., R. M. Iutzi, and A. J. H. McGaughey (2010). "Thermal conductivity and phonon transport in empty and water-filled carbon nanotubes". In: *Physical Review B - Condensed Matter and Materials Physics* 81.4, pp. 1–7. ISSN: 10980121. DOI: [10.1103/PhysRevB.81.045413](https://doi.org/10.1103/PhysRevB.81.045413).

- Tosi, N. et al. (2013). "Mantle dynamics with pressure- and temperature-dependent thermal expansivity and conductivity". In: *Physics of the Earth and Planetary Interiors* 217, pp. 48–58. ISSN: 00319201. DOI: [10.1016/j.pepi.2013.02.004](https://doi.org/10.1016/j.pepi.2013.02.004). URL: <http://dx.doi.org/10.1016/j.pepi.2013.02.004>.
- Trønnnes, R. G. (2009). "Structure, mineralogy and dynamics of the lowermost mantle". In: *Mineralogy and Petrology* 99, pp. 243–261. ISSN: 0930-0708. DOI: [10.1007/s00710-009-0068-z](https://doi.org/10.1007/s00710-009-0068-z). URL: <http://link.springer.com/10.1007/s00710-009-0068-z>.